BIT Numerical Mathematics (2026) 66:63
https://doi.org/10.1007/s10543-026-01158-0

BIT

A posteriori error estimates for mixed-dimensional Darcy flow using non-matching grids

Jhabriel Varela[1,2] · **Christian E. Schaerer**[1] · **Eirik Keilegavlen**[3] · **Inga Berre**[3]

Received: 9 December 2025 / Accepted: 5 October 2026
© The Author(s) 2026

Abstract
In this article, we extend the *a posteriori* error estimates for hierarchical mixed-dimensional elliptic equations developed in [Varela et al., *J. Numer. Math.*, 31 (2023), pp. 247–280] to the setting of non-matching mixed-dimensional grids. The extension is achieved by introducing transfer grids between the planar subdomain and interface grids, together with stable discrete projection operators for primal (potential) and dual (flux) variables and grid mismatch operators. The proposed estimators remain guaranteed, reliable and fully computable for locally mass-conservative approximations. Numerical experiments, including three-dimensional problems based on community benchmarks for incompressible Darcy flow in fractured porous media, demonstrate reliable performance of the estimators for the non-matching grids and effectivity that is comparable to the estimators previously obtained for matching grids.

Keywords A posteriori error estimates · Mixed-dimensional elliptic equations · Non-matching grids · Single phase flow in fractured porous media

Mathematics Subject Classification 65N15 · 65N50 · 76S05

✉ Inga Berre
inga.berre@uib.no

Jhabriel Varela
jhabriel@pol.una.py

Christian E. Schaerer
cschaer@pol.una.py

Eirik Keilegavlen
eirik.keilegavlen@uib.no

1 Polytechnic School, National University of Asunción, Campus de la UNA, P.O. Box 2111 SL, San Lorenzo, Paraguay

2 Polytechnic University Taiwan-Paraguay, Sebastián Gaboto - Comando de Comunicaciones del Ejército, P.O. Box 1018 AS, Asunción, Paraguay

3 Center for Modeling of Coupled Subsurface Dynamics, Department of Mathematics, University of Bergen, Allégaten 41, P.O. Box 7800 N-5020, Bergen, Norway

Published online: 26 October 2026

1 Introduction

The scalar hierarchical mixed-dimensional (mD) elliptic equation extends the standard Poisson equation by incorporating the coupling between domains of co-dimension one [1]. This framework is particularly well suited for modeling flow processes in fractured porous media [2, 3], where the rock matrix is represented as a 3D host domain, fractures as embedded 2D planar surfaces, fracture intersections as 1D line segments, and their intersections as 0D points. Over the past two decades, this model has been extensively studied, and a variety of techniques have been proposed to solve it; we refer the reader to the review articles [4, 5] and community benchmarks [6, 7] for comprehensive overviews. Notably, the model has been recently validated experimentally [8], further establishing its relevance and applicability.

Given that mD problems naturally span subdomains of different dimensions, it is both geometrically and computationally advantageous to discretize each subdomain with an independent grid, avoiding the constraints of matching grids. Previous works that have considered modeling and discretization of flow in fractured porous media on non-matching grids include [9–13]. In parallel, *a posteriori* error estimates were also developed for problems in mixed dimensions. For instance, [14] in the context of multi-scale mortar methods, [15–19] for Darcy flow in fractured media, and more recently [20] for hierarchical mD elliptic problems in the context of Darcy flow in networks of planar fractures. To our knowledge, however, no existing estimators cover the fully general mD setting—incorporating intersecting and fully embedded subdomains—on non-matching grids.

Motivated by filling this gap, we extend the estimates derived in [20] to the non-matching case. In our context, *non-matching* means that elements in the higher-dimensional grid, the lower-dimensional grid, or both, do not geometrically align with the elements of the coupling interface grid (also known as a mortar grid). However, it is important to remark that all these grids are individually conforming. Figure 1 illustrates this concept in two dimensions. Non-matching grids enable independent refinement or coarsening of subdomains and interfaces, potentially leading to significant computational savings. For instance, one may refine only one subdomain in response to large local estimator values, while leaving the others unchanged. Such fully disjoint adaptivity avoids the technical complexity of enforcing geometric inter-dimensional conformity.

Extending the validity of the *a posteriori* error estimators from the matching to the general non-matching case is a non-trivial task, as one needs to introduce appropriate mappings of the primal (potentials) and dual (fluxes) variables between subdomains and interfaces with different partitioning. In this work, we overcome this challenge by constructing a *transfer grid* (common refinement grid between subdomains and interfaces), from which potentials and interface fluxes are projected in an energy-consistent manner. This approach allows the estimates of [20] to carry over to the non-matching setting modulo the introduction of grid mismatch terms. Optimal generation of transfer grids, however, remains a challenging task [21–23].

The remainder of the article is organized as follows. In Sect. 2, we present the mD geometric decomposition together with the strong formulations. Section 3 introduces the functional framework, including local and mD spaces and continuous transfer

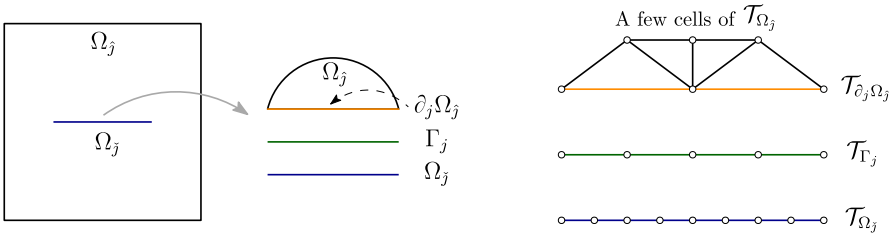


Fig. 1 Mixed-dimensional geometric setting. Left: A fracture $\Omega_{\check{\jmath}}$ fully embedded in the matrix $\Omega_{\hat{\jmath}}$. A close-up of the upper side of the fracture shows the interface Γ_j coupling $\Omega_{\check{\jmath}}$ and $\Omega_{\hat{\jmath}}$ through its internal boundary $\partial_j\Omega_{\hat{\jmath}}$. There exists a similar coupling on the lower side of the fracture, not shown in the figures. Right: A non-matching coupling between $\mathcal{T}_{\partial_j\Omega_{\hat{\jmath}}}$, $\mathcal{T}_{\Gamma_j}$ and $\mathcal{T}_{\Omega_{\check{\jmath}}}$. Grids are formally defined in Sect. 4.1

operators. Section 4 covers the discrete setting, formally introducing the grids, discrete projection and grid mismatch operators. In Sect. 5, we present the main *a posteriori* error bounds. Section 6 makes the error bounds concrete for primal and dual approximations and discusses potential and flux reconstructions. Finally, in Sect. 7, we present the numerical results and in Sect. 8 we draw our conclusions.

2 Mixed-dimensional setting and the model problem

In this section, we introduce the mD decomposition of the domain together with the strong forms of the model problem.

2.1 Mixed-dimensional decomposition

Following the notation introduced in [20], we consider an mD domain $Y \subset \mathbb{R}^n$, $n \in \{2, 3\}$ decomposed into strictly disjoint and flat subdomains Ω_i. Each Ω_i has a known dimension $d_i = d(i)$, where $0 \leq d_i \leq n$. There are N_Ω subdomains and we denote by $I = \{1, 2, \ldots, N_\Omega\}$ the index set of all subdomains. As shown in the left panel of Fig. 1, interfaces Γ_j establish the connection between two neighboring subdomains that are one dimension apart. Each interface has a known dimension $d_j = d(j)$, where $0 \leq d_j \leq n - 1$. There are N_Γ interfaces and the index set of interfaces is denoted by $J = \{1, 2, \ldots, N_\Gamma\}$. For a given interface Γ_j, we use the indices $\hat{\jmath} \in I$ and $\check{\jmath} \in I$ to respectively identify higher- and lower-dimensional neighboring subdomains $\Omega_{\hat{\jmath}}$ and $\Omega_{\check{\jmath}}$. The portion of the boundary of $\Omega_{\hat{\jmath}}$ geometrically coinciding with Γ_j is denoted by $\partial_j\Omega_{\hat{\jmath}}$. Throughout the article, we assume geometric compatibility of the coupling triplet $(\partial_j\Omega_{\hat{\jmath}}, \Gamma_j, \Omega_{\check{\jmath}})$ in the following sense.

Assumption 1 (Geometric compatibility of the coupling triplet) For each $j \in J$, the sets

$$\partial_j\Omega_{\hat{\jmath}}, \qquad \Gamma_j, \qquad \Omega_{\check{\jmath}}$$

have the same intrinsic dimension and are pairwise bi-Lipschitz equivalent. In particular, they are regarded as different representations of the same geometric object.

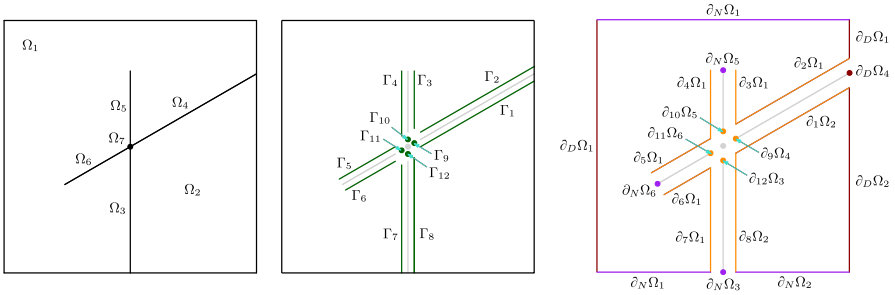


Fig. 2 Complete geometric decomposition of an mD domain. Left: Subdomains. Two 2D subdomains (Ω_1 and Ω_2) hosting four 1D fractures (Ω_3, Ω_4, Ω_5, Ω_6) that intersect at a common 0D point (Ω_7). Center: Interfaces. Twelve interfaces coupling neighboring subdomains of co-dimension one. Right: Internal and external boundary conditions

Given that several interfaces can be associated to a single subdomain, for all $i \in I$, we introduce the interface index sets $\hat{S}_i$ and $\check{S}_i$ to establish their connections. The set $\hat{S}_i$ contains the indices of all d_i-dimensional neighboring interfaces of Ω_i, whereas $\check{S}_i$ contains the indices of all $(d_i - 1)$-dimensional neighboring interfaces of Ω_i. For example, in Fig. 2, $\hat{S}_5 = \{4, 3\}$ and $\check{S}_5 = \{10\}$.

Recalling that $A \sqcup B$ denotes the disjoint union of the sets A and B, we define the set of all subdomains by $\Omega = \sqcup_{i\in I}\Omega_i$ and the set of all interfaces by $\Gamma = \sqcup_{j\in J}\Gamma_j$. Thus, a complete disjoint partitioning of the mD domain Y is given by $Y = \Omega \sqcup \Gamma$.

To finalize the geometric description, we define the boundary of Ω as $\partial\Omega = \partial_D\Omega \cup \partial_N\Omega \cup \partial_{\mathcal{I}}\Omega$, where $\partial_D\Omega = \cup_{i\in I}\partial_D\Omega_i$, $\partial_N\Omega = \cup_{i\in I}\partial_N\Omega_i$ and $\partial_{\mathcal{I}}\Omega = \cup_{i\in I}\cup_{j\in\hat{S}_i}\partial_j\Omega_i$ are respectively the Dirichlet, Neumann and internal portions of $\partial\Omega$, assumed to be strictly non-overlapping. Since the problem we are interested in is purely elliptic, we require $\partial_D\Omega \neq \emptyset$. A full geometric decomposition of an mD domain $Y \subset \mathbb{R}^2$ is shown schematically in Fig. 2.

2.2 The model problem

We now present the mD elliptic problem in strong form, in the context of incompressible single phase flow in fractured porous media. For the details, we refer to [2, 3, 24].

Problem 1 (Strong primal form) *Let $i \in I$ and $j \in J$. Then, find each pressure $p_i : \Omega_i \to \mathbb{R}$, such that*

$$-\nabla_i \cdot (\mathcal{K}_i \nabla_i p_i) + \sum_{j\in\hat{S}_i} \kappa_j \left(p_{\check{\jmath}} - p_{\hat{\jmath}}\right) = f_i \qquad \text{in } \Omega_i, \tag{1a}$$

$$\left(\mathcal{K}_{\hat{\jmath}} \nabla_{\hat{\jmath}} p_{\hat{\jmath}}\right) \cdot \boldsymbol{n}_{\hat{\jmath}} = \kappa_j \left(p_{\check{\jmath}} - p_{\hat{\jmath}}\right) \qquad \text{on } \partial_j\Omega_{\hat{\jmath}}, \tag{1b}$$

$$(\mathcal{K}_i \nabla_i p_i) \cdot \boldsymbol{n}_i = 0 \qquad \text{on } \partial_N\Omega_i, \tag{1c}$$

$$p_i = g_{D,i} \qquad \text{on } \partial_D\Omega_i. \tag{1d}$$

Introducing the subdomain Darcy (tangential) flux $\boldsymbol{u}_i = -\mathcal{K}_i \nabla_i p_i$ and the interface (normal) flux $\lambda_j = -\kappa_j(p_{\check{j}} - p_{\hat{j}})$, Problem 1 can be recast into the following dual problem.

Problem 2 (Strong dual form) *Let $i \in I$ and $j \in J$. Then, find each Darcy flux $\boldsymbol{u}_i : \Omega_i \to \mathbb{R}^{d_i}$, interface flux $\lambda_j : \Gamma_j \to \mathbb{R}$, and pressure $p_i : \Omega_i \to \mathbb{R}$, such that*

$$\nabla_i \cdot \boldsymbol{u}_i - \sum_{j \in \hat{S}_i} \lambda_j = f_i \quad \text{in } \Omega_i, \tag{2a}$$

$$\boldsymbol{u}_i = -\mathcal{K}_i \nabla_i p_i \quad \text{in } \Omega_i, \tag{2b}$$

$$\lambda_j = -\kappa_j(p_{\check{j}} - p_{\hat{j}}) \quad \text{on } \Gamma_j, \tag{2c}$$

$$\boldsymbol{u}_{\hat{j}} \cdot \boldsymbol{n}_{\hat{j}} = \lambda_j \quad \text{on } \partial_j \Omega_{\hat{j}}, \tag{2d}$$

$$\boldsymbol{u}_i \cdot \boldsymbol{n}_i = 0 \quad \text{on } \partial_N \Omega_i, \tag{2e}$$

$$p_i = g_{D,i} \quad \text{on } \partial_D \Omega_i. \tag{2f}$$

In Problems 1 and 2, ∇_i is the d_i-dimensional *nabla* operator, $\boldsymbol{n}_i$ the outward-pointing normal vector on a given Neumann boundary $\partial_N \Omega_i$ or internal boundary $\partial_{\mathcal{I}} \Omega_i$, $f_i : \Omega_i \to \mathbb{R}$ is a source term, and $g_{D,i} : \partial_D \Omega_i \to \mathbb{R}$ is the Dirichlet boundary data. Finally, $\mathcal{K}_i : \Omega_i \to \mathbb{R}^{d_i \times d_i}$ is the effective permeability matrix and $\kappa_j : \Gamma_j \to \mathbb{R}$ is the effective normal permeability. For the physical interpretation of the model, the reader is referred to [3, 20, 25] and the references therein.

Remark 1 The dual form provides a natural framework for coupling non-matching grids, since the introduction of the interface flux λ_j naturally decouples subdomain and interface contributions while strongly imposing inter-dimensional flux continuity.

3 Functional framework

We now define the functional spaces required to formulate the weak versions of Problems 1 and 2, respectively. From this point onward, we shall use $\nabla_i(\cdot)$ and $\nabla_i \cdot (\cdot)$ to denote the d_i-dimensional weak gradient and divergence operators, respectively.

3.1 Local and global spaces

Let S denote an open and bounded domain. We use $L^2(S)$ to denote the space of square-integrable functions on S, equipped with inner product $(\cdot,\cdot)_S \equiv (\cdot,\cdot)_{L^2(S)}$ and norm $\|\cdot\|_S \equiv \|\cdot\|_{L^2(S)}$. We also introduce the space of square-integrable vector-valued functions on S, that is $\mathbf{L}^2(S) = [L^2(S)]^{d(S)}$, with $d(S)$ denoting the intrinsic dimension of S. For the sake of compactness we also use $(\cdot,\cdot)_S \equiv (\cdot,\cdot)_{\mathbf{L}^2(S)}$ and $\|\cdot\|_S \equiv \|\cdot\|_{\mathbf{L}^2(S)}$ in the vector case.

The standard energy space is defined as $H^1(\Omega_i) = \{q_i \in L^2(\Omega_i) : \nabla_i q_i \in \mathbf{L}^2(\Omega_i)\}$ while $H^1_0(\Omega_i) = \{q_i \in H^1(\Omega_i) : q_i|_{\partial_D \Omega_i} = 0\}$ denotes the subspace of $H^1(\Omega_i)$ of functions with vanishing traces on Dirichlet boundaries. Additionally, we let $g_i \in$

$H^1(\Omega_i)$ represent any function whose restriction on $\partial_D\Omega_i$ matches the boundary data, i.e., $g_i|_{\partial_D\Omega_i} = g_{D,i}$. Here, $(\ \cdot\ )|_{\partial_D\Omega_i} : H^1(\Omega_i) \to H^{1/2}(\partial_D\Omega_i)$ is the trace operator with $H^{1/2}(\partial_D\Omega_i)$ denoting the fractional Sobolev space on the Dirichlet boundary. We also define the local affine space whose trace on $\partial_D\Omega_i$ satisfies the Dirichlet boundary data as $H^1_0(\Omega_i) + g_i = \{\tilde{w}_i = w_i + g_i : w_i \in H^1_0(\Omega_i)\}$. Although implicit, notice that traces on internal boundaries also belong to the space $H^{1/2}(\partial_{\mathcal{I}}\Omega_i)$.

We now turn our focus to the flux spaces. Define the space $\mathbf{H}(\mathrm{div}, \Omega_i) = \{\boldsymbol{v}_i \in \mathbf{L}^2(\Omega_i) : \nabla_i \cdot \boldsymbol{v}_i \in L^2(\Omega_i)\}$ alongside the subspace $\mathbf{V}_i = \{\boldsymbol{v}_i \in \mathbf{H}(\mathrm{div}, \Omega_i) : (\boldsymbol{v}_i \cdot \boldsymbol{n}_i)|_{\partial_N\Omega_i} = 0\}$, which enforces vanishing traces on Neumann boundaries. Similarly, the space $\mathbf{V}_{0,i} = \{\boldsymbol{v}_i \in \mathbf{V}_i : (\boldsymbol{v}_i \cdot \boldsymbol{n}_i)|_{\partial_{\mathcal{I}}\Omega_i} = 0\}$ consists of functions with vanishing traces on both Neumann and internal boundaries. To handle internal boundaries, following [24], we introduce the linear extension operator $\mathcal{R}_j : L^2(\Gamma_j) \to \mathbf{V}_{\hat{\jmath}}$, satisfying for any $\nu_j \in L^2(\Gamma_j)$:

$$(\mathcal{R}_j\nu_j)|_{\partial_j\Omega_{\hat{\jmath}}} \cdot \boldsymbol{n}_{\hat{\jmath}} = \begin{cases} \nu_j & \text{on } \partial_j\Omega_{\hat{\jmath}}, \\ 0 & \partial\Omega_{\hat{\jmath}} \setminus \partial_j\Omega_{\hat{\jmath}} \end{cases}. \tag{3}$$

An explicit form for $\mathcal{R}_j$ can be obtained by solving an auxiliary elliptic problem [24]. We shall revisit this operator at the end of Sect. 3.2. The space $\mathbf{V}_{0,i}$, together with the linear extension operator $\mathcal{R}_j$, allow us to represent, in a weak sense, subdomain fluxes $\boldsymbol{v}_i \in \mathbf{V}_i$ with $(\boldsymbol{v}_i \cdot \boldsymbol{n}_i)|_{\partial_j\Omega_{\hat{\jmath}}} = \nu_j$ for all $j \in \check{S}_i$, as $\boldsymbol{v}_i = \boldsymbol{v}_{0,i} + \sum_{j\in\check{S}_i} \mathcal{R}_j\nu_j$, with $\boldsymbol{v}_{0,i} \in \mathbf{V}_{0,i}$ and $\nu_j \in L^2(\Gamma_j)$. The above decomposition suggests the following local space for subdomain fluxes

$$\mathbf{X}_i := \mathbf{V}_{0,i} \times \prod_{j\in\check{S}_i} \mathcal{R}_j L^2(\Gamma_j). \tag{4}$$

Remark 2 *($\mathbf{X}_i$ vs. $\mathbf{V}_i$)* The space $\mathbf{X}_i$ has higher regularity compared to $\mathbf{V}_i$, as this latter does not contain L^2 traces on internal boundaries. This enhanced regularity on internal boundaries allows the construction of pure L^2-type projections on coupling triplets in the case of weak dual approximations.

Global spaces are now immediate by taking the Cartesian product of local spaces,

$$L^2(\Omega) := \prod_{i\in I} L^2(\Omega_i), \qquad L^2(\Gamma) := \prod_{j\in J} L^2(\Gamma_j). \tag{5}$$

Analogous definitions hold for $\mathbf{L}^2(\Omega)$, $H^1(\Omega)$, $H^1_0(\Omega)$, $H^1_0(\Omega) + g$, $H^{1/2}(\partial_D\Omega)$, $\mathbf{V}$, $\mathbf{V}_0$, and $\mathbf{X}$. We will later use these spaces to represent weak solutions to the model problem in the mD partition $\Omega \sqcup \Gamma$.

3.2 Continuous transfer operators

Let $j \in J$ and consider the coupling triplet $(\partial_j\Omega_{\hat{\jmath}}, \Gamma_j, \Omega_j)$. Recall that by Assumption 1, the three sets represent the same geometric domain.

Definition 1 (Continuous transfer operators) We define the following bounded linear transfer operators:

(i) Transfers between $\partial_j\Omega_{\hat{\jmath}}$ and Γ_j:

$$\mathcal{P}_{\hat{\jmath}}^{j} : H^{1/2}(\partial_j\Omega_{\hat{\jmath}}) \longrightarrow H^{1/2}(\Gamma_j), \qquad \mathcal{D}_{j}^{\hat{\jmath}} : L^2(\Gamma_j) \longrightarrow L^2(\partial_j\Omega_{\hat{\jmath}}),$$

where $\mathcal{P}_{\hat{\jmath}}^{j}$ is an $H^{1/2}$-identification and $\mathcal{D}_{j}^{\hat{\jmath}}$ is an L^2-identification.

(ii) Transfers between $\Omega_{\check{\jmath}}$ and Γ_j:

$$\mathcal{P}_{\check{\jmath}}^{j} : H^{1}(\Omega_{\check{\jmath}}) \longrightarrow H^{1/2}(\Gamma_j), \qquad \mathcal{D}_{j}^{\check{\jmath}} : L^2(\Gamma_j) \longrightarrow L^2(\Omega_{\check{\jmath}}),$$

where $\mathcal{P}_{\check{\jmath}}^{j}$ is the standard embedding $H^1(\Omega_{\check{\jmath}}) \hookrightarrow H^{1/2}(\Gamma_j)$ on the same domain and $\mathcal{D}_{j}^{\check{\jmath}}$ is an L^2-identification.

The operators $\mathcal{D}_{j}^{\hat{\jmath}}$ and $\mathcal{D}_{j}^{\check{\jmath}}$ preserve the L^2 norm under identification:

$$\|\mathcal{D}_{j}^{\hat{\jmath}}\nu\|_{\partial_j\Omega_{\hat{\jmath}}} = \|\nu\|_{\Gamma_j}, \qquad \|\mathcal{D}_{j}^{\check{\jmath}}\nu\|_{\Omega_{\check{\jmath}}} = \|\nu\|_{\Gamma_j},$$

while the operator $\mathcal{P}_{\hat{\jmath}}^{j}$ preserves the $H^{1/2}$ norm under identification

$$\|\mathcal{P}_{\hat{\jmath}}^{j} q\|_{H^{1/2}(\Gamma_j)} = \|q\|_{H^{1/2}(\partial_j\Omega_{\hat{\jmath}})}.$$

The operator $\mathcal{P}_{\check{\jmath}}^{j}$ is stable under the Sobolev embedding $H^1(\Omega_{\check{\jmath}}) \hookrightarrow H^{1/2}(\Gamma_j)$ on the same domain

$$\|\mathcal{P}_{\check{\jmath}}^{j} q\|_{H^{1/2}(\Gamma_j)} \le C_{\mathrm{emb}}\, \|q\|_{H^{1}(\Omega_{\check{\jmath}})}.$$

Here, $\|\cdot\|_{H^1(S)}$ and $\|\cdot\|_{H^{1/2}(S)}$ are the usual Sobolev norms on S [26], and C_{emb} is the continuity constant of the embedding $H^1(S) \hookrightarrow H^{1/2}(S)$; see, e.g., [27, Ch. 4, Prop. 4.4].

Remark 3 *(Continuous transfers vs. discrete projections)* The operators $\mathcal{P}$ and $\mathcal{D}$ above act as canonical identifications on the common geometry (with norms associated to the target space). They are introduced to keep notation aligned with the discrete non-matching case (where genuine projections $\widetilde{\mathcal{P}}$ and $\widetilde{\mathcal{D}}$ are required), and in Sect. 4.3.1, to define the grid mismatch operators.

With the interface to internal-boundary L^2-transfer $\mathcal{D}_{j}^{\hat{\jmath}}(\cdot)$ defined, the subdomain extension can be written as the following composition:

$$\mathcal{R}_j = \mathcal{R}_j^{*} \circ \mathcal{D}_{j}^{\hat{\jmath}} : L^2(\Gamma_j) \longrightarrow L^2(\partial_j\Omega_{\hat{\jmath}}) \longrightarrow \mathbf{V}_{\hat{\jmath}}, \tag{6}$$

where $\mathcal{R}_j^{*}$ is any bounded lifting from the internal boundary into $\mathbf{V}_{\hat{\jmath}}$ (cf. [24]).

3.3 Weak forms

Before stating the weak primal and dual forms of Problems 1 and 2, we make the data regularity explicit in the following assumption. Here and in the following, we shall use the notation $[\ \cdot\ ]$ to denote an ordered collection of subdomain and/or interface variables, depending on context.

Assumption 2 *(Data regularity)*

(i) $f = [f_i] \in L^2(\Omega)$.
(ii) $g_D = [g_{D,i}] \in H^{1/2}(\partial_D\Omega)$.
(iii) For all $i \in I$, $\mathcal{K}_i$ is bounded, positive definite and satisfies the usual ellipticity condition

$$c_{\mathcal{K}_i}^2|\boldsymbol{\xi}|^2 \le \mathcal{K}_i\boldsymbol{\xi}\cdot\boldsymbol{\xi} \le C_{\mathcal{K}_i}^2|\boldsymbol{\xi}|^2, \qquad \forall \boldsymbol{\xi} \in \mathbb{R}^{d_i}.$$

(iv) For all $j \in J$, κ_j is non-degenerate with bounds

$$0 < c_{\kappa_j} \le \kappa_j \le C_{\kappa_j} < \infty.$$

Later, we shall use $c_{\mathcal{K}_i}|_S$ to denote the restriction of $c_{\mathcal{K}_i}(\mathbf{x})$ on the domain S.

Problem 3 (Weak primal form) *Let $p = [p_i]$ and $g = [g_i] \in H^1(\Omega)$. Then, given $f = [f_i] \in L^2(\Omega)$, find $p \in H_0^1(\Omega) + g$ such that*

$$\sum_{i\in I}(\mathcal{K}_i\nabla_i p_i, \nabla_i q_i)_{\Omega_i} + \sum_{j\in J}\left(\kappa_j(\mathcal{P}_{\check{j}}^j p_{\check{j}} - \mathcal{P}_{\hat{j}}^j p_{\hat{j}}|_{\partial_j\Omega_{\hat{j}}}), \mathcal{P}_{\check{j}}^j q_{\check{j}} - \mathcal{P}_{\hat{j}}^j q_{\hat{j}}|_{\partial_j\Omega_{\hat{j}}}\right)_{\Gamma_j}$$
$$= \sum_{i\in I}(f_i, q_i)_{\Omega_i} \qquad \forall q = [q_i] \in H_0^1(\Omega). \tag{7}$$

Remark 4 *(Well-posedness of the primal form)* The bilinear form associated with the primal weak form is symmetric and, provided Assumption 2 holds, coercive on $H_0^1(\Omega)$. Consequently, the problem is well-posed and equivalent to finding the unique minimizer $p \in H_0^1(\Omega) + g$ of the energy functional:

$$\mathcal{J}(q) = \frac{1}{2}\sum_{i\in I}\left\|\mathcal{K}_i^{1/2}\nabla_i q_i\right\|_{\Omega_i}^2 + \frac{1}{2}\sum_{j\in J}\left\|\kappa_j^{1/2}(\mathcal{P}_{\check{j}}^j q_{\check{j}} - \mathcal{P}_{\hat{j}}^j q_{\hat{j}}|_{\partial_j\Omega_{\hat{j}}})\right\|_{\Gamma_j}^2 - \sum_{i\in I}(f_i, q_i)_{\Omega_i}.$$

Problem 4 (Dual weak form) *Let $\boldsymbol{u} = [\boldsymbol{u}_{0,i}, \lambda_j]$ and $p = [p_i]$. Then, given $f = [f_i] \in L^2(\Omega)$ and $g_D = [g_{D,i}] \in H^{1/2}(\partial_D\Omega)$, find $\boldsymbol{u} \in \mathbf{X}$ and $p \in L^2(\Omega)$ such that*

$$\sum_{i\in I}\left(\mathcal{K}_i^{-1}\left(\boldsymbol{u}_{0,i} + \textstyle\sum_{j\in\check{S}_i}\mathcal{R}_j^*\circ\mathcal{D}_j^{\hat{j}}\lambda_j\right), \boldsymbol{v}_{0,i} + \textstyle\sum_{j\in\check{S}_i}\mathcal{R}_j^*\circ\mathcal{D}_j^{\hat{j}}v_j\right)_{\Omega_i}$$
$$- \sum_{i\in I}\left(p_i, \nabla_i\cdot\left(\boldsymbol{v}_{0,i} + \textstyle\sum_{j\in\check{S}_i}\mathcal{R}_j^*\circ\mathcal{D}_j^{\hat{j}}v_j\right) + \textstyle\sum_{j\in\hat{S}_i}\mathcal{D}_j^{\check{j}}v_j\right)_{\Omega_i} + \sum_{j\in J}\left(\kappa_j^{-1}\lambda_j, v_j\right)_{\Gamma_j}$$
$$= -\sum_{i\in I}\left(g_{D,i}, (\boldsymbol{v}_{0,i}\cdot\boldsymbol{n}_i)|_{\partial_D\Omega_i}\right)_{\partial_D\Omega_i} \qquad \forall \boldsymbol{v} = [\boldsymbol{v}_{0,i}, v_j] \in \mathbf{X}. \tag{8a}$$

$$\sum_{i\in I}\left(\nabla_i\cdot\left(\boldsymbol{u}_{0,i}+\textstyle\sum_{j\in\check{S}_i}\mathcal{R}_j^*\circ\mathcal{D}_j^{\hat{j}}\lambda_j\right),q_i\right)_{\Omega_i}-\sum_{i\in I}\left(\textstyle\sum_{j\in\hat{S}_i}\mathcal{D}_j^{\check{j}}\lambda_j,q_i\right)_{\Omega_i}$$
$$=\sum_{i\in I}(f_i,q_i)_{\Omega_i}\qquad\forall q=[q_i]\in L^2(\Omega). \tag{8b}$$

Remark 5 *(Well-posedness of the dual form)* The dual form exhibits a saddle-point structure. Well-posedness can be proven using inf-sup arguments [24], provided the data satisfies Assumption 2.

We will employ mD energy norms to measure the deviation between the exact weak solutions and admissible approximations. More precisely, for an mD potential function $q=[q_i]\in H_0^1(\Omega)$, we define

$$|||q|||^2=\sum_{i\in I}\left\|\mathcal{K}_i^{1/2}\nabla_i q_i\right\|_{\Omega_i}^2+\sum_{j\in J}\left\|\kappa_j^{1/2}\left(\mathcal{P}_{\check{j}}^j q_{\check{j}}-\mathcal{P}_{\hat{j}}^j q_{\hat{j}|\partial_j\Omega_j}\right)\right\|_{\Gamma_j}^2, \tag{9}$$

and for an mD flux function $\boldsymbol{v}=[\boldsymbol{v}_{0,i},v_j]\in\mathbf{L}^2(\Omega)\times L^2(\Gamma)$, we define the energy norm

$$|||\boldsymbol{v}|||_*^2=\sum_{i\in I}\left\|\mathcal{K}_i^{-1/2}\left(\boldsymbol{v}_{0,i}+\textstyle\sum_{j\in\check{S}_i}\mathcal{R}_j^*\circ\mathcal{D}_j^{\hat{j}}v_j\right)\right\|_{\Omega_i}^2+\sum_{j\in J}\left\|\kappa_j^{-1/2}v_j\right\|_{\Gamma_j}^2. \tag{10}$$

We will use both norms to present the guaranteed upper bounds on the primal (the mD potential) and dual (the mD flux) variables in Sect. 5.

4 Discrete setting

In this section, we formally introduce the grids and define the discrete projection and grid mismatch operators. To treat the most general range of dimensionalities, our exposition assumes Y such that $\min_{i\in I}d_i=0$ and $\max_{i\in I}d_i=n=3$.

4.1 Grid definitions

For all $i\in I$, we denote by $\mathcal{T}_{\Omega_i}$ a simplicial and strictly non-overlapping partition of Ω_i, such that

$$\overline{\Omega_i}=\bigcup_{K\in\mathcal{T}_{\Omega_i}}K,\qquad\dim(K)\in\{0,1,2,3\}.$$

Similarly, for all $j\in J$, we denote by $\mathcal{T}_{\Gamma_j}$ a simplicial and strictly non-overlapping partition of Γ_j, such that

$$\overline{\Gamma_j}=\bigcup_{K\in\mathcal{T}_{\Gamma_j}}K,\qquad\dim(K)\in\{0,1,2\}.$$

Let e denote a face from the set of faces $\mathcal{E}_K$ of an element $K \in \mathcal{T}_{\Omega_i}$. For a fixed $j \in J$, we define the internal boundary grid as

$$\mathcal{T}_{\partial_j\Omega_{\hat{j}}} := \left(\bigcup_{K\in\mathcal{T}_{\Omega_j}} \bigcup_{e\in\mathcal{E}_K} e \right) \bigcap \partial_j\Omega_{\hat{j}}, \qquad \overline{\partial_j\Omega_{\hat{j}}} = \bigcup_{K\in\mathcal{T}_{\partial_j\Omega_{\hat{j}}}} K, \qquad \dim(K) \in \{0,1,2\}.$$

As illustrated in the right panel of Fig. 1, we allow the grid triplet $(\mathcal{T}_{\partial_j\Omega_{\hat{j}}}, \mathcal{T}_{\Gamma_j}, \mathcal{T}_{\Omega_i})$ to be non-matching. When necessary, we shall use K_X to denote an element of any admissible grid $\mathcal{T}_X$.

To ensure the stability of the discrete projection operators for the primal problem that will be constructed in Sect. 4.2.1, we require all partitions of subdomains and interfaces to be shape-regular.

Assumption 3 *(Shape-regularity of mixed-dimensional meshes)* There exists $\vartheta > 0$ such that every simplex K in each mesh $\mathcal{T}_{\Omega_i}, \mathcal{T}_{\Gamma_j}, \mathcal{T}_{\partial_j\Omega_{\hat{j}}}$ satisfies $h_K/\rho_K \leq \vartheta$, where h_K is the diameter and ρ_K the inradius of K. All meshes are conforming on their respective domains.

Before defining the discrete projection operators, we need to introduce the *transfer grid* between subdomain and interface grids. This grid facilitates the coupling of non-matching grids by resolving the geometric mismatch between them. We focus our exposition on the 3D case (2D interface grid) as the 2D case (1D interface grid) involves fewer geometric complexities.

Definition 2 *(Transfer grid)* Let $j \in J$ and $(\mathcal{T}_{\partial_j\Omega_{\hat{j}}}, \mathcal{T}_{\Gamma_j}, \mathcal{T}_{\Omega_{\hat{j}}})$ be a coupling grid triplet. We construct the transfer grid $\mathcal{T}_{\Gamma_j,X}$ with $X \in \{\partial_j\Omega_{\hat{j}}, \Omega_{\hat{j}}\}$ via a two-step process. First, identify the set of nodes $\mathcal{V}_{\Gamma_j,X} = \mathcal{V}_{\Gamma_j} \bigcup \mathcal{V}_X$ of the transfer grid, with $\mathcal{V}_{\Gamma_j}$ and $\mathcal{V}_X$ denoting the set of nodes of $\mathcal{T}_{\Gamma_j}$ and $\mathcal{T}_X$, respectively. Next, for each pair of elements K_{Γ_j} and K_X, define

$$S_{\Gamma_j,X} := K_{\Gamma_j} \bigcap K_X. \tag{11}$$

The above intersections result in one of the following three cases:

(i) *Polygonal domain*. If $S_{\Gamma_j,X}$ is a triangle, then $K_{\Gamma_j,X} := S_{\Gamma_j,X}$, and we include it directly in $\mathcal{T}_{\Gamma_j,X}$. Otherwise, $S_{\Gamma_j,X}$ is a non-simplex macro-element and it must be triangulated into simplicial elements, see e.g., [28].
(ii) *Line segment*. If $S_{\Gamma_j,X}$ is a line-segment, it represents a shared boundary between two elements and does not contribute as an element to $\mathcal{T}_{\Gamma_j,X}$.
(iii) *Empty intersection*. If $S_{\Gamma_j,X}$ is void, we ignore it.

Figure 3 shows examples of 1D (top panel) and 2D (bottom panel) transfer grids. To finalize this section, we summarize the geometric properties of the transfer grid.

Remark 6 *(Properties of the transfer grid)* The transfer grid $\mathcal{T}_{\Gamma_j,X}$ has the properties of node inclusion, refinement, dimensionality, and partitioning:

(i) $\mathcal{V}_{\Gamma_j} \subseteq \mathcal{V}_{\Gamma_j,X}, \mathcal{V}_X \subseteq \mathcal{V}_{\Gamma_j,X}$.

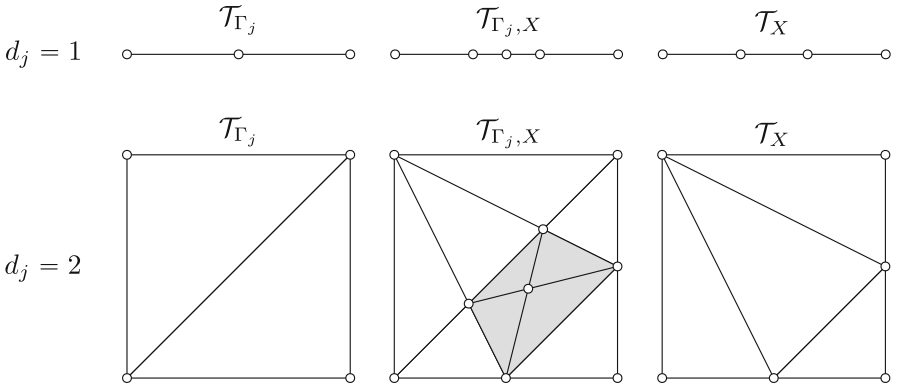


Fig. 3 Transfer grids $\mathcal{T}_{\Gamma_j,X}$ coupling interface grids $\mathcal{T}_{\Gamma_j}$ with $\mathcal{T}_X$, $X \in \{\partial_j\Omega_{\hat{j}}, \Omega_{\hat{j}}\}$. Top: 1D coupling. Bottom: 2D coupling. The shaded quadrilateral corresponds to a macro-element $S_{\Gamma_j,X}$ that was further refined into four simplices using its barycenter coordinate

(ii) $\left|\mathcal{T}_{\Gamma_j}\right| \leq \left|\mathcal{T}_{\Gamma_j,X}\right|, |\mathcal{T}_X| \leq \left|\mathcal{T}_{\Gamma_j,X}\right|$.
(iii) For all $K \in \mathcal{T}_{\Gamma_j,X}$, $\dim(K) = d_j$.
(iv) By Assumption 1, $\overline{\Gamma_j} = \bigcup_{K\in\mathcal{T}_{\Gamma_j,X}} K$, $\overline{X} = \bigcup_{K\in\mathcal{T}_{\Gamma_j,X}} K$.

In Remark 6 (ii), $|\cdot|$ denotes the cardinality of the mesh, i.e., the number of simplicial elements K.

4.2 Discrete projection operators

To define the discrete projection operators, we shall make extensive use of the broken spaces of polynomials. For $k \geq 0$ and any mesh $\mathcal{T}_X$ on a geometric set X, we define

$$\mathbb{P}_k(\mathcal{T}_X) := \{\, q_h \in L^2(X) \;:\; q_h|_K \in \mathbb{P}_k(K) \;\; \forall\, K \in \mathcal{T}_X \,\}. \tag{12}$$

Functions in $\mathbb{P}_k(\mathcal{T}_X)$ are generally discontinuous across inter-element boundaries and are not required to satisfy any external boundary condition.

4.2.1 Discrete projections for the primal problem

The projection of potentials for the weak primal problem on non-matching grids is carried out in two stages. First, potentials defined on the source grids (the internal boundary grids and lower-dimensional subdomain grids) are prolonged onto the corresponding transfer grids. Second, the potentials are projected onto the target interface grid using the Scott-Zhang quasi-interpolant [29].

To be precise, let $j \in J$ be fixed and let $(\partial_j\Omega_{\hat{j}}, \Gamma_j, \Omega_{\hat{j}})$ be a coupling triplet satisfying Assumption 1 and let Assumption 3 also be satisfied. For $k \geq 1$, we define the prolongation operators

$$\widetilde{\mathcal{P}}_{\hat{j}}^{j,\hat{j}} : \mathbb{P}_k(\mathcal{T}_{\partial_j\Omega_{\hat{j}}}) \cap H^{1/2}(\partial_j\Omega_{\hat{j}}) \longrightarrow \mathbb{P}_k(\mathcal{T}_{\Gamma_j,\partial_j\Omega_{\hat{j}}}) \cap H^{1/2}(\partial_j\Omega_{\hat{j}}), \tag{13a}$$

$$\widetilde{\mathcal{P}}_{\check{j}}^{j,\check{J}} : \mathbb{P}_k(\mathcal{T}_{\Omega_{\check{j}}}) \cap (H^1(\Omega_{\check{j}}) + g_{\check{j}}) \longrightarrow \mathbb{P}_k(\mathcal{T}_{\Gamma_j,\Omega_{\check{j}}}) \cap (H^1(\Omega_{\check{j}}) + g_{\check{j}}), \tag{13b}$$

where the transfer grids $\mathcal{T}_{\Gamma_j,\partial_j\Omega_{\hat{j}}}$ and $\mathcal{T}_{\Gamma_j,\Omega_{\check{j}}}$ are defined as in Definition 2. Two remarks are in order. First, the intersection of a broken polynomial space $\mathbb{P}_k$ with an $H^{1/2}$-space selects the conforming C^0 finite element subspace, since jump discontinuities across inter-element boundaries are not admissible in $H^{1/2}$. Second, whenever $\Omega_{\check{j}}$ intersects the external Dirichlet boundary, we assume that the prescribed boundary datum $g_{\check{j}}$ is exactly representable in the corresponding conforming polynomial space. Under this assumption, the affine spaces in (13b) are nonempty and the boundary condition is imposed exactly. The case in which the discrete approximation does not satisfy the Dirichlet boundary condition exactly is outside the scope of the present work; for related discussion in the context of functional a posteriori estimates, see [30, Sec. 4].

Since $\mathcal{T}_{\Gamma_j,X}$ is a subdivision of $\mathcal{T}_X$, for any potential $q_h \in \mathbb{P}_k(\mathcal{T}_{\partial_j\Omega_{\hat{j}}}) \cap H^{1/2}(\partial_j\Omega_{\hat{j}})$, (13a) satisfies

$$(\widetilde{\mathcal{P}}_{\hat{j}}^{j,\hat{J}} q_h)|_{K_{\Gamma_j,\partial_j\Omega_{\hat{j}}}} = q_h|_{K_{\partial_j\Omega_{\hat{j}}}}, \qquad \forall K_{\Gamma_j,\partial_j\Omega_{\hat{j}}} \in S_{\Gamma_j,\partial_j\Omega_{\hat{j}}}, \tag{14}$$

for each transfer macro-element $S_{\Gamma_j,\partial_j\Omega_{\hat{j}}}$ and for each $K_{\partial_j\Omega_{\hat{j}}} \subseteq S_{\Gamma_j,\partial_j\Omega_{\hat{j}}}$. The operator $\widetilde{\mathcal{P}}_{\check{j}}^{j,\check{J}}$ from (13b) satisfies an analogous property for potentials defined on $\mathcal{T}_{\Omega_{\check{j}}}$.

Once functions have been prolonged to the transfer grids, we project them onto the target interface grid:

$$\widetilde{\mathcal{P}}_{j,\hat{j}}^{j} : \mathbb{P}_k(\mathcal{T}_{\Gamma_j,\partial_j\Omega_{\hat{j}}}) \cap H^{1/2}(\partial_j\Omega_{\hat{j}}) \longrightarrow \mathbb{P}_k(\mathcal{T}_{\Gamma_j}) \cap H^{1/2}(\Gamma_j), \tag{15a}$$

$$\widetilde{\mathcal{P}}_{j,\check{j}}^{j} : \mathbb{P}_k(\mathcal{T}_{\Gamma_j,\Omega_{\check{j}}}) \cap (H^1(\Omega_{\check{j}}) + g_{\check{j}}) \longrightarrow \mathbb{P}_k(\mathcal{T}_{\Gamma_j}) \cap H^{1/2}(\Gamma_j). \tag{15b}$$

Here, $\widetilde{\mathcal{P}}_{j,\hat{j}}^{j}$ and $\widetilde{\mathcal{P}}_{j,\check{j}}^{j}$ denote Scott-Zhang quasi-interpolators constructed on $\mathcal{T}_{\Gamma_j}$, see [29] for the details.

Definition 3 *(Discrete projections for the primal problem)* Let $j \in J$ and consider the coupling triplet $(\partial_j\Omega_{\hat{j}}, \Gamma_j, \Omega_{\check{j}})$. For a fixed degree $k \geq 1$, the discrete projections for the weak primal problem are given by the following compositions

$$\widetilde{\mathcal{P}}_{\hat{j}}^{j} := \widetilde{\mathcal{P}}_{j,\hat{j}}^{j} \circ \widetilde{\mathcal{P}}_{\hat{j}}^{j,\hat{j}}, \tag{16a}$$

$$\widetilde{\mathcal{P}}_{\check{j}}^{j} := \widetilde{\mathcal{P}}_{j,\check{j}}^{j} \circ \widetilde{\mathcal{P}}_{\check{j}}^{j,\check{j}}. \tag{16b}$$

The following lemma establishes a key stability result for the projection operators.

Lemma 1 (Stability of discrete projection operators for the weak primal problem) *Let $j \in J$ and $k \geq 1$. Then, the operators $\widetilde{\mathcal{P}}_{\hat{j}}^{j}$ and $\widetilde{\mathcal{P}}_{\check{j}}^{j}$ in (16b) are linear and bounded:*

$$\|\widetilde{\mathcal{P}}_{\hat{j}}^{j} q_h\|_{H^{1/2}(\Gamma_j)} \leq C_1 \|q_h\|_{H^{1/2}(\partial_j\Omega_{\hat{j}})}, \qquad \|\widetilde{\mathcal{P}}_{\check{j}}^{j} \phi_h\|_{H^{1/2}(\Gamma_j)} \leq C_2 \|\phi_h\|_{H^1(\Omega_{\check{j}})},$$

with constants C_1 and C_2 depending only on the shape-regularity of the target interface grid and on the polynomial degree k.

Proof The prolongation operators are isometric identifications on an equal or more refined partition of the same domain; thus norm preserving in H^s, $s \in [0,1]$ (see e.g., [31, 32]). The Scott-Zhang quasi-interpolant on the target interface grid is linear and H^s-stable for $s \in [0,1]$ [29]. Setting $s = 1/2$ yields the first bound. For the second bound, use the Scott-Zhang stability with $s = 1$ and then the continuous embedding $H^1(\Gamma_j) \hookrightarrow H^{1/2}(\Gamma_j)$, cf. Section 4.8 of [33]. □

We emphasize that the stability results in Lemma 1 (and for the ones from the next section) are independent from the transfer grids, as they act purely as data identifiers (stability constants equal to one). This result is numerically verified in Sect. 7.1.

4.2.2 Discrete projections for the dual problem

We construct discrete projections for interface fluxes onto the internal boundary $\mathcal{T}_{\partial_j\Omega_{\hat{\jmath}}}$ and the lower-dimensional grid $\mathcal{T}_{\Omega_{\check{\jmath}}}$, while preserving the elementwise mass on the target grids. The construction consists of (i) a prolongation to a transfer grid and (ii) an agglomeration on the target grid via a constrained L^2 projection enforcing cell mean.

Fix $j \in J$ and the coupling triplet $(\partial_j\Omega_{\hat{\jmath}}, \Gamma_j, \Omega_{\check{\jmath}})$ with transfer grids $\mathcal{T}_{\Gamma_j,\partial_j\Omega_{\hat{\jmath}}}$ and $\mathcal{T}_{\Gamma_j,\Omega_{\check{\jmath}}}$ from Definition 2. For $k \geq 0$ and $v_h \in \mathbb{P}_k(\mathcal{T}_{\Gamma_j})$, define the elementwise prolongations

$$\widetilde{\mathcal{D}}_j^{j,\hat{\jmath}} : \mathbb{P}_k(\mathcal{T}_{\Gamma_j}) \longrightarrow \mathbb{P}_k(\mathcal{T}_{\Gamma_j,\partial_j\Omega_{\hat{\jmath}}}), \tag{17a}$$

$$\widetilde{\mathcal{D}}_j^{j,\check{\jmath}} : \mathbb{P}_k(\mathcal{T}_{\Gamma_j}) \longrightarrow \mathbb{P}_k(\mathcal{T}_{\Gamma_j,\Omega_{\check{\jmath}}}), \tag{17b}$$

by elementwise value restriction: $(\cdot)|_{S_{\Gamma_j,X}} = (\cdot)|_{K_{\Gamma_j}}$ for each macro-element $S_{\Gamma_j,X} \subset K_{\Gamma_j}$ and $X \in \{\partial_j\Omega_{\hat{\jmath}}, \Omega_{\check{\jmath}}\}$. Note that the functions prolonged to the transfer grid are in general discontinuous across transfer elements.

Given the prolonged data v_h on $\mathcal{T}_{\Gamma_j,X}$ for $X \in \{\partial_j\Omega_{\hat{\jmath}}, \Omega_{\check{\jmath}}\}$, we perform a constrained L^2 agglomeration on the target cell $K \in \mathcal{T}_X$. Let $\{\phi_i^K\}_{i=1}^{N_k}$ be a basis of $\mathbb{P}_k(K)$. Define the local system $M^K\alpha^K = b^K$, where

$$M_{ij}^K = (\phi_i^K, \phi_j^K)_K, \qquad b_i^K = (v_h, \phi_i^K)_K = \textstyle\sum_{K_{\Gamma_j,X} \subset K} (v_h, \phi_i^K)_{K_{\Gamma_j,X}} \tag{18}$$

$$c_i^K = (1, \phi_i^K)_K, \qquad m^K = \textstyle\sum_{K_{\Gamma_j,X} \subset K} (v_h, 1), \tag{19}$$

with M^K denoting the local mass matrix, b^K the vector of constants, and c^K and m^K the mass constraints. The coefficients α^K and the Lagrange multiplier μ^K are determined from the local constrained optimization problem

$$\begin{bmatrix} M^K & c^K \\ (c^K)^\top & 0 \end{bmatrix} \begin{bmatrix} \alpha^K \\ \mu^K \end{bmatrix} = \begin{bmatrix} b^K \\ m^K \end{bmatrix}. \tag{20}$$

The unique solvability of this system is guaranteed for any $k \geq 0$. The local mass matrix M^K is symmetric positive definite and since $1 \in \mathbb{P}_k(K)$, the constraint vector

c^K is non-zero. This ensures the satisfaction of the inf-sup condition for the Lagrange multiplier μ^K. This local constrained optimization problem defines the operators

$$\widetilde{\mathcal{D}}^{\hat{\jmath}}_{j,\hat{\jmath}} : \mathbb{P}_k(\mathcal{T}_{\Gamma_j,\partial_j\Omega_{\hat{\jmath}}}) \longrightarrow \mathbb{P}_k(\mathcal{T}_{\partial_j\Omega_{\hat{\jmath}}}), \tag{21a}$$

$$\widetilde{\mathcal{D}}^{\check{\jmath}}_{j,\check{\jmath}} : \mathbb{P}_k(\mathcal{T}_{\Gamma_j,\Omega_{\check{\jmath}}}) \longrightarrow \mathbb{P}_k(\mathcal{T}_{\Omega_{\check{\jmath}}}), \tag{21b}$$

where, on each target element K, the image is the unique polynomial in $\mathbb{P}_k(K)$ determined by the constrained local problem (20). Consequently, the resulting polynomial on K is $(\widetilde{\mathcal{D}}^{\hat{\jmath}}_{j,\hat{\jmath}}\nu_h)|_K = \sum_{i=1}^{N_k} \alpha_i^K \phi_i^K$ and analogously for $\widetilde{\mathcal{D}}^{\check{\jmath}}_{j,\check{\jmath}}(\cdot)$ on $\mathcal{T}_{\Omega_{\check{\jmath}}}$.

Definition 4 *(Discrete projections of interface fluxes for the dual problem)* Let $j \in J$ and consider the coupling triplet $(\partial_j\Omega_{\hat{\jmath}}, \Gamma_j, \Omega_{\check{\jmath}})$. For a fixed degree $k \geq 0$, the discrete projections of interface fluxes for the weak dual problem are given by compositions

$$\widetilde{\mathcal{D}}^{\hat{\jmath}}_{j} := \widetilde{\mathcal{D}}^{\hat{\jmath}}_{j,\hat{\jmath}} \circ \widetilde{\mathcal{D}}^{j,\hat{\jmath}}_{j}, \tag{22a}$$

$$\widetilde{\mathcal{D}}^{\check{\jmath}}_{j} := \widetilde{\mathcal{D}}^{\check{\jmath}}_{j,\check{\jmath}} \circ \widetilde{\mathcal{D}}^{j,\check{\jmath}}_{j}. \tag{22b}$$

The resulting mapping preserves elementwise mass and inherits stability from the constrained L^2 projection.

Lemma 2 (Stability of discrete projections of interface fluxes for the dual problem) *The operators $\widetilde{\mathcal{D}}^{\hat{\jmath}}_{j}$ and $\widetilde{\mathcal{D}}^{\check{\jmath}}_{j}$ are linear, L^2–stable, and satisfy*

$$\|\widetilde{\mathcal{D}}^{\hat{\jmath}}_{j}\nu_h\|_{\partial_j\Omega_{\hat{\jmath}}} \leq C_3 \|\nu_h\|_{\Gamma_j}, \qquad \|\widetilde{\mathcal{D}}^{\check{\jmath}}_{j}\nu_h\|_{\Omega_{\check{\jmath}}} \leq C_4 \|\nu_h\|_{\Gamma_j}, \tag{23}$$

with positive constants C_3 and C_4. Moreover, for each $K \in \mathcal{T}_{\partial_j\Omega_{\hat{\jmath}}}$, the local polynomial $(\widetilde{\mathcal{D}}^{\hat{\jmath}}_{j}\nu_h)|_K$ is characterized as the unique solution of the constrained minimization problem

$$(\widetilde{\mathcal{D}}^{\hat{\jmath}}_{j}\nu_h)|_K = \arg\min_{\varphi\in\mathbb{P}_k(K)} \left\{ \|\varphi - \nu_h\|_K : (\varphi, 1)_K = m^K \right\}, \tag{24}$$

and an analogous statement holds for $\widetilde{\mathcal{D}}^{\check{\jmath}}_{j}(\cdot)$ on $\mathcal{T}_{\Omega_{\check{\jmath}}}$.

Proof The prolongation step acts as an isometric identification on each transfer subelement and is therefore L^2-stable. The agglomeration onto the target grid is a constrained L^2–orthogonal projection, hence locally stable and the best-approximation property holds by orthogonality. Global bounds follow from the fact that, for each target element $K \in \mathcal{T}_X$, $X \in \{\partial_j\Omega_{\hat{\jmath}}, \Omega_{\check{\jmath}}\}$, only finitely many transfer elements $K_{\Gamma_j,X} \subset K$ contribute to the local projection. □

Importantly, the discrete projection operator $\widetilde{\mathcal{D}}^{\hat{\jmath}}_{j}$ is locally mass-conservative, in the sense that for any $\nu_h \in \mathbb{P}_k(\mathcal{T}_{\Gamma_j})$, there holds

$$(\widetilde{\mathcal{D}}^{\hat{\jmath}}_{j}\nu_h, 1)_K = m^K \quad \text{with} \quad m^K = \sum_{K_{\Gamma_j,X}\subset K} (\nu_h, 1)_{K_{\Gamma_j,X}}. \tag{25}$$

That is, the total interface flux over K equals the sum of incoming fluxes on all transfer grid elements $K_{\Gamma_j,\partial_j\Omega_j}$ contained in K. The same property holds for $\widetilde{\mathcal{D}}_j^{\check{j}}(\cdot)$ on $\mathcal{T}_{\Omega_j}$.

Remark 7 *(Discrete projections of interface fluxes for dual approximations of the lowest-order)* In the lowest-order case $k = 0$, (20) reduces to the overlap-weighted average on each target element:

$$(\widetilde{\mathcal{D}}_{j,\hat{j}}^{\hat{j}}\nu_h)|_K = \frac{1}{|K|}\sum_{K_{\Gamma_j,\partial_j\Omega_{\hat{j}}}\subset K}(\nu_h,1)_{K_{\Gamma_j,\partial_j\Omega_{\hat{j}}}} = \frac{1}{|K|}\sum_{K_{\Gamma_j,\partial_j\Omega_{\hat{j}}}\subset K}|K_{\Gamma_j,\partial_j\Omega_{\hat{j}}}|\,\nu_h|_{K_{\Gamma_j,\partial_j\Omega_{\hat{j}}}}.$$

An analogous property holds for projection onto the low-dimensional subdomain grid.

Figure 4 shows the four discrete projection operators introduced in this section.

4.3 Grid mismatch operators

This subsection introduces the grid mismatch (GM) operators required to evaluate the local error indicators in Sect. 5. Each GM operator quantifies the discrepancy between a continuous transfer operator from Definition 1 and its discrete realization from Sects. 4.2.1–4.2.2 on a non-matching coupling triplet $(\partial_j\Omega_{\hat{j}}, \Gamma_j, \Omega_{\check{j}})$. We also

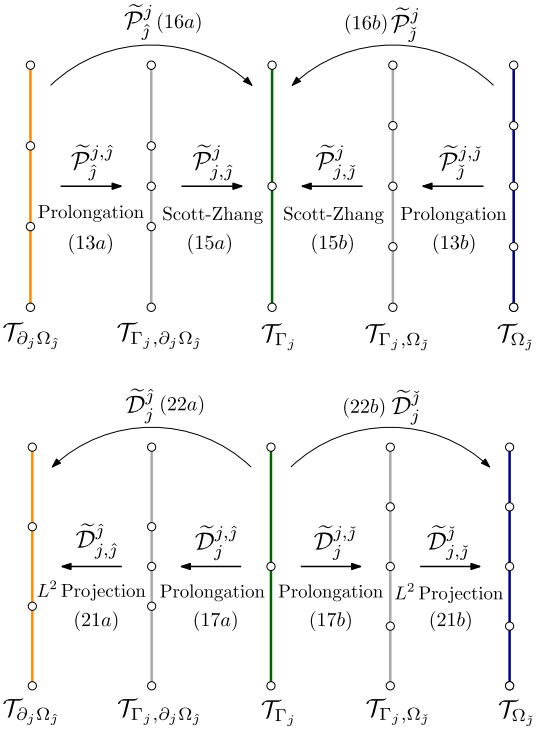


Fig. 4 Schematic representation of the discrete projection operators for the weak primal and dual problems. In each case, the construction is decomposed into a prolongation to a transfer grid followed by a projection onto the target grid. Curved arrows indicate the corresponding composite discrete operators. Equation numbers refer to the formal definitions in the text

fix the convention by which the discrete lifting acts on grid-mismatch data, and prove a cellwise mass-defect property essential for the proof of Theorem 1.

4.3.1 Defect operators

Let $j \in J$ and consider the coupling triplet $(\partial_j\Omega_{\hat{\jmath}}, \Gamma_j, \Omega_{\check{\jmath}})$. The defect operators are constructed on the transfer grids of Definition 2 as the difference between a continuous transfer operator and its discrete realization. Before stating the construction, we recall a key structural property of the transfer grids.

Remark 8 *(Transfer grids as common refinements)* By Remark 6, the transfer grids satisfy $\mathcal{V}_{\Gamma_j} \cup \mathcal{V}_{\partial_j\Omega_{\hat{\jmath}}} \subseteq \mathcal{V}_{\Gamma_j,\partial_j\Omega_{\hat{\jmath}}}$ and $\mathcal{V}_{\Gamma_j} \cup \mathcal{V}_{\Omega_{\check{\jmath}}} \subseteq \mathcal{V}_{\Gamma_j,\Omega_{\check{\jmath}}}$, that is, $\mathcal{T}_{\Gamma_j,\partial_j\Omega_{\hat{\jmath}}}$ and $\mathcal{T}_{\Gamma_j,\Omega_{\check{\jmath}}}$ are the *common refinements* of the interface grid $\mathcal{T}_{\Gamma_j}$ with the internal-boundary grid $\mathcal{T}_{\partial_j\Omega_{\hat{\jmath}}}$ and with the lower-dimensional subdomain grid $\mathcal{T}_{\Omega_{\check{\jmath}}}$, respectively. Consequently, any piecewise polynomial on $\mathcal{T}_{\Gamma_j}$ admits a pointwise-equal representation as a piecewise polynomial on $\mathcal{T}_{\Gamma_j,\partial_j\Omega_{\hat{\jmath}}}$ (and on $\mathcal{T}_{\Gamma_j,\Omega_{\check{\jmath}}}$), and the same holds for any piecewise polynomial on $\mathcal{T}_{\partial_j\Omega_{\hat{\jmath}}}$ or $\mathcal{T}_{\Omega_{\check{\jmath}}}$. The transfer grids are therefore the natural common partitions on which the continuous identifications $\mathcal{D}$, $\mathcal{P}$ and the discrete realizations $\widetilde{\mathcal{D}}$, $\widetilde{\mathcal{P}}$ admit a simultaneous, pointwise-well-defined representation, so that their pointwise difference is unambiguously a piecewise polynomial on the corresponding transfer grid.

Definition 5 *(Grid mismatch operators)* For $q_{\hat{\jmath}} \in \mathbb{P}_k(\mathcal{T}_{\partial_j\Omega_{\hat{\jmath}}}) \cap H^{1/2}(\partial_j\Omega_{\hat{\jmath}})$, $q_{\check{\jmath}} \in \mathbb{P}_k(\Omega_{\check{\jmath}}) \cap (H^1(\Omega_{\check{\jmath}}) + g_{\check{\jmath}})$ and $\nu_j \in \mathbb{P}_k(\mathcal{T}_{\Gamma_j})$, the primal and dual grid-mismatch operators associated with the coupling triplet $(\partial_j\Omega_{\hat{\jmath}}, \Gamma_j, \Omega_{\check{\jmath}})$ are defined elementwise on the transfer grids by

$$\delta\mathcal{P}^j_{\hat{\jmath}} q_{\hat{\jmath}} := (\mathcal{P}^j_{\hat{\jmath}} q_{\hat{\jmath}} - \widetilde{\mathcal{P}}^j_{\hat{\jmath}} q_{\hat{\jmath}}) \in \mathbb{P}_k(\mathcal{T}_{\Gamma_j,\partial_j\Omega_{\hat{\jmath}}}) \cap H^{1/2}(\mathcal{T}_{\Gamma_j,\partial_j\Omega_{\hat{\jmath}}}), \quad k \geq 1, \tag{26a}$$

$$\delta\mathcal{P}^j_{\check{\jmath}} q_{\check{\jmath}} := (\mathcal{P}^j_{\check{\jmath}} q_{\check{\jmath}} - \widetilde{\mathcal{P}}^j_{\check{\jmath}} q_{\check{\jmath}}) \in \mathbb{P}_k(\mathcal{T}_{\Gamma_j,\Omega_{\check{\jmath}}}) \cap H^{1/2}(\mathcal{T}_{\Gamma_j,\Omega_{\check{\jmath}}}), \quad k \geq 1, \tag{26b}$$

$$\delta\mathcal{D}^{\hat{\jmath}}_j \nu_j := (\mathcal{D}^{\hat{\jmath}}_j \nu_j - \widetilde{\mathcal{D}}^{\hat{\jmath}}_j \nu_j) \in \mathbb{P}_k(\mathcal{T}_{\Gamma_j,\partial_j\Omega_{\hat{\jmath}}}), \quad k \geq 0, \tag{26c}$$

$$\delta\mathcal{D}^{\check{\jmath}}_j \nu_j := (\mathcal{D}^{\check{\jmath}}_j \nu_j - \widetilde{\mathcal{D}}^{\check{\jmath}}_j \nu_j) \in \mathbb{P}_k(\mathcal{T}_{\Gamma_j,\Omega_{\check{\jmath}}}), \quad k \geq 0, \tag{26d}$$

where, in each formula, both terms on the right-hand side are evaluated on the transfer grid in the sense of Remark 8: the continuous identification $\mathcal{P}^j_\bullet q_i$ (resp. $\mathcal{D}^\bullet_j \nu_j$) is the piecewise polynomial on the source grid prolonged elementwise to the transfer grid, and the discrete realization $\widetilde{\mathcal{P}}^j_\bullet q_i$ (resp. $\widetilde{\mathcal{D}}^\bullet_j \nu_j$) is the piecewise polynomial on the target grid prolonged back elementwise to the transfer grid.

By Remark 8, both prolongations to the transfer grid are isometric identifications: they preserve the L^2 (resp. $H^{1/2}$) norm and introduce no information loss. The defect operators in Definition 5 are therefore well-defined pointwise on their respective transfer grids and vanish identically in the matching case $\mathcal{T}_{\partial_j\Omega_{\hat{\jmath}}} = \mathcal{T}_{\Gamma_j} = \mathcal{T}_{\Omega_{\check{\jmath}}}$ (see also Corollary 1). Their stability follows from the triangle inequality applied to the underlying continuous identifications (cf. Definition 1) and discrete projections (cf. Lemmas 1 and 2).

4.3.2 Lifting of grid mismatch data

The local GM error indicators that will be presented in Theorem 1 contain the bulk lift $\widetilde{\mathcal{R}}_j^* \circ \delta\mathcal{D}_j^{\hat{\jmath}}\nu_j$. The discrete lift $\widetilde{\mathcal{R}}_j^*$ is, by construction in [24], defined on functions in $\mathbb{P}_k(\mathcal{T}_{\partial_j\Omega_{\hat{\jmath}}})$, whereas $\delta\mathcal{D}_j^{\hat{\jmath}}\nu_j$, by (26c), can in general only be resolved on the finer transfer grid $\mathcal{T}_{\Gamma_j,\partial_j\Omega_{\hat{\jmath}}}$. To resolve this domain mismatch, we abuse notation and adopt the convention that $\widetilde{\mathcal{R}}_j^*$ acts on transfer-grid data by precomposition with the constrained L^2 projection $\widetilde{\mathcal{D}}_{j,\hat{\jmath}}^{\hat{\jmath}}$ from Sect. 4.2.2.

Definition 6 *(Lifting of grid mismatch data)* For $w \in \mathbb{P}_k(\mathcal{T}_{\Gamma_j,\partial_j\Omega_{\hat{\jmath}}})$, the lift of w into the bulk subdomain $\Omega_{\hat{\jmath}}$ is defined as

$$\widetilde{\mathcal{R}}_j^*(w) \;:=\; \widetilde{\mathcal{R}}_j^*\big(\widetilde{\mathcal{D}}_{j,\hat{\jmath}}^{\hat{\jmath}}\, w\big) \;\in\; \mathbf{V}_{h,\hat{\jmath}}, \tag{27}$$

where $\mathbf{V}_{h,\hat{\jmath}}$ is a suitable discrete subspace of $\mathbf{V}_{\hat{\jmath}}$.

The convention (27) is well-posed because $\widetilde{\mathcal{D}}_{j,\hat{\jmath}}^{\hat{\jmath}}$ is the orthogonal L^2 projection from a refinement of $\mathcal{T}_{\partial_j\Omega_{\hat{\jmath}}}$ onto $\mathcal{T}_{\partial_j\Omega_{\hat{\jmath}}}$ itself, and is therefore L^2-stable with constant equal to one,

$$\|\widetilde{\mathcal{D}}_{j,\hat{\jmath}}^{\hat{\jmath}}\, w\|_{\partial_j\Omega_{\hat{\jmath}}} \;\le\; \|w\|_{\partial_j\Omega_{\hat{\jmath}}}, \qquad w \in \mathbb{P}_k(\mathcal{T}_{\Gamma_j,\partial_j\Omega_{\hat{\jmath}}}). \tag{28}$$

Composition with $\widetilde{\mathcal{R}}_j^*$ therefore introduces no nonexplicit constant: the lift (27) inherits the computability of $\widetilde{\mathcal{R}}_j^*$ on its native domain $\mathbb{P}_k(\mathcal{T}_{\partial_j\Omega_j})$.

We further require the discrete lift to be *locally compatible* with the source-boundary data, in the following sense.

Assumption 4 *(Cell-balance of the discrete lift)* For every $w \in \mathbb{P}_k(\mathcal{T}_{\partial_j\Omega_j})$ and every $K \in \mathcal{T}_{\Omega_j}$, the discrete lift satisfies

$$\Big(\widetilde{\mathcal{R}}_j^*(w)\cdot \boldsymbol{n}_K,\, 1\Big)_{\partial K} \;=\; (w,1)_{\partial K\cap\partial_j\Omega_j}. \tag{29}$$

Assumption 4 states that, on every bulk simplex K, the lifted function transports source-boundary data into the interior with no net flux contribution from any face of ∂K that does not lie on $\partial_j\Omega_{\hat{\jmath}}$. The discrete Raviart-Thomas-based lift constructed in [24] satisfies Assumption 4, since by construction it assigns zero face moments on every face of ∂K outside $\partial_j\Omega_{\hat{\jmath}}$, and in particular zero face mean. Other H(div)-conforming discrete lifts that share this structural property also fall within the scope of the framework.

4.3.3 Cellwise mass-defect property

The proof of Theorem 1 relies on a cellwise vanishing property of the grid-mismatch residual that follows from the mean-preserving construction of the discrete projections in Sect. 4.2.2 and from Assumption 4 on the discrete lift. We isolate this property in the following lemma, which we will invoke in Appendix A.

Lemma 3 (Cellwise mass-defect property of the grid-mismatch residual) *Let* $\boldsymbol{v} = [\boldsymbol{v}_{0,i}, v_j] \in \mathbf{X}_h$ *(a suitable finite-dimensional subspace of* $\mathbf{X}$*) and define the grid-mismatch residual on each subdomain* Ω_i, $i \in I$, *by*

$$\rho_i \;:=\; \nabla_i \cdot \sum_{j\in\check{S}_i} \widetilde{\mathcal{R}}_j^{*} \circ \delta\mathcal{D}_j^{\hat{j}} v_j \;+\; \sum_{j\in\hat{S}_i} \delta\mathcal{D}_j^{\check{j}} v_j, \tag{30}$$

where $\widetilde{\mathcal{R}}_j^{*}$ *is interpreted on transfer-grid data via the convention* (27)*. Then*

$$(\rho_i, 1)_K \;=\; 0 \qquad \forall\, K \in \mathcal{T}_{\Omega_i},\; i \in I. \tag{31}$$

Proof The two contributions to ρ_i are treated separately.

For the lower-dimensional term, we fix $j \in \hat{S}_i$, so that $i = \check{j}$, and let $K \in \mathcal{T}_{\Omega_j}$. By the mean-preserving property of the constrained L^2 projection $\widetilde{\mathcal{D}}_j^{\check{j}}$ established in Lemma 2,

$$\left(\widetilde{\mathcal{D}}_j^{\check{j}} v_j, 1\right)_K \;=\; \sum_{K_{\Gamma_j,\Omega_{\check{j}}}\subset K} \left(v_j, 1\right)_{K_{\Gamma_j,\Omega_{\check{j}}}} \;=\; \left(\mathcal{D}_j^{\check{j}} v_j, 1\right)_K,$$

where the second equality uses that the canonical L^2 identification $\mathcal{D}_j^{\check{j}} v_j$ on $K \in \mathcal{T}_{\Omega_{\check{j}}}$ is given by the integral of v_j over the union of transfer cells $K_{\Gamma_j,\Omega_{\check{j}}} \subset K$. Subtracting yields $\left(\delta\mathcal{D}_j^{\check{j}} v_j, 1\right)_K = 0$.

For the bulk term, we fix $j \in \check{S}_i$, so that $i = \hat{j}$, and let $K \in \mathcal{T}_{\Omega_{\hat{j}}}$. By the convention (27), the lift acts on transfer-grid data through the constrained projection $\widetilde{\mathcal{D}}_{j,\hat{j}}^{\hat{j}}$, and Assumption 4 applied to the discrete data $w := \widetilde{\mathcal{D}}_{j,\hat{j}}^{\hat{j}}\big(\delta\mathcal{D}_j^{\hat{j}} v_j\big) \in \mathbb{P}_k(\mathcal{T}_{\partial_j\Omega_{\hat{j}}})$ gives

$$\left(\nabla_i \cdot \widetilde{\mathcal{R}}_j^{*} \circ \delta\mathcal{D}_j^{\hat{j}} v_j, 1\right)_K \;=\; \sum_{e\subset\partial K\cap\partial_j\Omega_{\hat{j}}} \left(\widetilde{\mathcal{D}}_{j,\hat{j}}^{\hat{j}}\, \delta\mathcal{D}_j^{\hat{j}} v_j, 1\right)_e.$$

Each face $e \subset \partial K \cap \partial_j\Omega_{\hat{j}}$ is an element of the internal boundary grid $\mathcal{T}_{\partial_j\Omega_{\hat{j}}}$ (since the latter is the trace of $\mathcal{T}_{\Omega_{\hat{j}}}$ on $\partial_j\Omega_{\hat{j}}$), so the constrained L^2 projection $\widetilde{\mathcal{D}}_{j,\hat{j}}^{\hat{j}}$ preserves the face mean of its argument:

$$\left(\widetilde{\mathcal{D}}_{j,\hat{j}}^{\hat{j}}\, \delta\mathcal{D}_j^{\hat{j}} v_j, 1\right)_e \;=\; \left(\delta\mathcal{D}_j^{\hat{j}} v_j, 1\right)_e \;=\; \left(\mathcal{D}_j^{\hat{j}} v_j, 1\right)_e - \left(\widetilde{\mathcal{D}}_j^{\hat{j}} v_j, 1\right)_e \;=\; 0,$$

where the last equality uses Lemma 2 (mean-preserving property of $\widetilde{\mathcal{D}}_j^{\hat{j}}$ on $\mathcal{T}_{\partial_j\Omega_{\hat{j}}}$). Summing over all faces $e \subset \partial K \cap \partial_j\Omega_{\hat{j}}$ gives $\left(\nabla_i \cdot \widetilde{\mathcal{R}}_j^{*} \circ \delta\mathcal{D}_j^{\hat{j}} v_j, 1\right)_K = 0$. Adding the two cellwise vanishing identities yields (31). □

5 A posteriori error estimation

In this section, we focus on the a posteriori analysis on non-matching grids. We start by introducing the admissible mD functions that can be used to estimate the errors, then we present our main result: the *a posteriori* error bounds on non-matching grids. Finally, we introduce error indicators that will be employed in the numerical examples.

5.1 Admissible mixed-dimensional pairs on non-matching grids

The functional estimates below are stated for comparison pairs that are conforming in the energy spaces, locally conservative on the non-matching grid, and compatible with the computable transfer operators entering the estimator. The construction of such pairs from particular numerical methods is discussed in the next section.

Let $Q_h^g \subset H_0^1(\Omega) + g$ be a finite-dimensional affine space of conforming mD potentials, and let $\mathbf{X}_h \subset \mathbf{X}$ be a finite-dimensional space of conforming mD fluxes, both associated with the non-matching mD partition of $Y = \Omega \sqcup \Gamma$. We assume that the restrictions and traces of functions in Q_h^g, and the interface components of functions in $\mathbf{X}_h$, are compatible with the discrete projection and grid mismatch operators introduced in Sect. 4.

Definition 7 *(Locally conservative flux on a non-matching grid)* Let $\boldsymbol{v} = [\boldsymbol{v}_{0,i}, v_j] \in \mathbf{X}_h$. For each $i \in I$, define the non-matching residual

$$\widetilde{r}_i(\boldsymbol{v}; f) := f_i - \nabla_i \cdot \left(\boldsymbol{v}_{0,i} + \textstyle\sum_{j \in \check{S}_i} \widetilde{\mathcal{R}}_j^* \circ \widetilde{\mathcal{D}}_j^{\hat{j}} v_j\right) + \textstyle\sum_{j \in \hat{S}_i} \widetilde{\mathcal{D}}_j^{\check{j}} v_j.$$

We say that $\boldsymbol{v}$ is locally conservative on the non-matching grid if

$$\left(\widetilde{r}_i(\boldsymbol{v}; f), 1\right)_K = 0 \qquad \forall K \in \mathcal{T}_{\Omega_i}, \quad \forall i \in I.$$

The corresponding admissible class is

$$\mathbf{X}_{h,\mathrm{LC}}(f) := \left\{\boldsymbol{v} \in \mathbf{X}_h : \left(\widetilde{r}_i(\boldsymbol{v}; f), 1\right)_K = 0 \quad \forall K \in \mathcal{T}_{\Omega_i}, \quad \forall i \in I\right\}.$$

Note that to satisfy Definition 7 on non-matching grids, the discrete projection operators $\widetilde{\mathcal{D}}_j^{\hat{j}}$ and $\widetilde{\mathcal{D}}_j^{\check{j}}$ (cf. Section 4.2.2) play a key role, as their construction guarantees inter-dimensional mass conservation.

Definition 8 *(Admissible mD pair on non-matching grids)* A pair $(q, \boldsymbol{v}) \in Q_h^g \times \mathbf{X}_h$ is called admissible on the non-matching grid if

$$\boldsymbol{v} \in \mathbf{X}_{h,\mathrm{LC}}(f),$$

and all transferred, lifted, and defect quantities entering the majorant are well defined and finite. In particular, the quantities

$$\widetilde{\mathcal{P}}_{\hat{j}}^{j} q_{\hat{j}}, \quad \widetilde{\mathcal{P}}_{\check{j}}^{j} q_{\check{j}}, \quad \delta\mathcal{P}_{\hat{j}}^{j} q_{\hat{j}}, \quad \delta\mathcal{P}_{\check{j}}^{j} q_{\check{j}},$$

and

$$\widetilde{\mathcal{D}}_j^{\hat{j}} v_j, \quad \widetilde{\mathcal{D}}_j^{\check{j}} v_j, \quad \delta\mathcal{D}_j^{\hat{j}} v_j, \quad \delta\mathcal{D}_j^{\check{j}} v_j$$

are well defined for every coupling triplet, and the lifted defect fields and their elementwise divergences belong to the required L^2 spaces.

5.2 Main results

The following theorem presents the main result of this work.

Theorem 1 (Guaranteed upper bounds on non-matching grids) *For every $q \in Q_h^g$ and every $\boldsymbol{v} \in \mathbf{X}_{h,\mathrm{LC}}(f)$ in the sense of Definition 8, define the majorant as*

$$\mathcal{M}(q, \boldsymbol{v}, f) := \eta_{\mathrm{NM,R}}(\boldsymbol{v}, f) + \eta_{\mathrm{GM,R}}(\boldsymbol{v}) + \eta_{\mathrm{NM,DF}}(q, \boldsymbol{v}) + \eta_{\mathrm{GM,DF}}(q, \boldsymbol{v}), \tag{32}$$

with the global indicators

$$\eta^2_{\mathrm{NM,R}}(\boldsymbol{v}, f) = \sum_{i\in I} \sum_{K\in\mathcal{T}_{\Omega_i}} \eta^2_{\mathrm{NM,R},K}, \tag{33a}$$

$$\eta^2_{\mathrm{GM,R}}(\boldsymbol{v}) = \sum_{i\in I} \sum_{K\in\mathcal{T}_{\Omega_i}} \eta^2_{\mathrm{GM,R},K}, \tag{33b}$$

$$\eta^2_{\mathrm{NM,DF}}(q, \boldsymbol{v}) = \sum_{i\in I} \sum_{K\in\mathcal{T}_{\Omega_i}} \eta^2_{\mathrm{NM,DF}_\parallel,K} + \sum_{j\in J} \sum_{K\in\mathcal{T}_{\Gamma_j}} \eta^2_{\mathrm{NM,DF}_\perp,K}, \tag{33c}$$

$$\eta^2_{\mathrm{GM,DF}}(q, \boldsymbol{v}) = \sum_{i\in I} \sum_{K\in\mathcal{T}_{\Omega_i}} \eta^2_{\mathrm{GM,DF}_\parallel,K} + \sum_{j\in J} \sum_{K\in\mathcal{T}_{\Gamma_j}} \eta^2_{\mathrm{GM,DF}_\perp,K}, \tag{33d}$$

and the local error estimators given by

$$\eta_{\mathrm{NM,DF}_\parallel,K} = \left\| \mathcal{K}_i^{-1/2} \left(\boldsymbol{v}_{0,i} + \textstyle\sum_{j\in\check{S}_i} \widetilde{\mathcal{R}}_j^* \circ \widetilde{\mathcal{D}}_j^{\hat{j}} v_j \right) + \mathcal{K}_i^{1/2} \nabla_i q_i \right\|_K, \tag{34a}$$

$$\eta_{\mathrm{NM,DF}_\perp,K} = \left\| \kappa_j^{-1/2} v_j + \kappa_j^{1/2} \left(\widetilde{\mathcal{P}}_j^j q_{\check{j}} - \widetilde{\mathcal{P}}_{\hat{j}}^j q_{\hat{j}} \right) \right\|_K, \tag{34b}$$

$$\eta_{\mathrm{NM,R},K} = \frac{h_K}{\pi c_{\mathcal{K}_i,K}} \left\| f_i - \nabla_i \cdot \left(\boldsymbol{v}_{0,i} + \textstyle\sum_{j\in\check{S}_i} \widetilde{\mathcal{R}}_j^* \circ \widetilde{\mathcal{D}}_j^{\hat{j}} v_j \right) + \sum_{j\in\hat{S}_i} \widetilde{\mathcal{D}}_j^{\check{j}} v_j \right\|_K, \tag{34c}$$

$$\eta_{\mathrm{GM,DF}_\parallel,K} = \left\| \mathcal{K}_i^{-1/2} \textstyle\sum_{j\in\check{S}_i} \widetilde{\mathcal{R}}_j^* \circ \delta\mathcal{D}_j^{\hat{j}} v_j \right\|_K, \tag{34d}$$

$$\eta_{\mathrm{GM,DF}_\perp,K} = \left\| \kappa_j^{1/2} \left(\delta\mathcal{P}_j^j q_{\check{j}} - \delta\mathcal{P}_{\hat{j}}^j q_{\hat{j}} \right) \right\|_K, \tag{34e}$$

$$\eta_{\mathrm{GM,R},K} = \frac{h_K}{\pi c_{\mathcal{K}_i,K}} \left\| \nabla_i \cdot \textstyle\sum_{j\in\check{S}_i} \widetilde{\mathcal{R}}_j^* \circ \delta\mathcal{D}_j^{\hat{j}} v_j + \sum_{j\in\hat{S}_i} \delta\mathcal{D}_j^{\check{j}} v_j \right\|_K. \tag{34f}$$

Then, the following estimates hold:

(i) Let $p = [p_i] \in H_0^1(\Omega) + g$ be the solution of Problem 3. Then

$$|||p - q||| \leq \mathcal{M}(q, \boldsymbol{v}, f) =: \mathcal{M}_p^{\oplus} \qquad \forall \boldsymbol{v} \in \mathbf{X}_{h,\mathrm{LC}}(f). \tag{35}$$

(ii) Let $\boldsymbol{u} = [\boldsymbol{u}_{0,i}, \lambda_j] \in \mathbf{X}$ be the solution of Problem 4. Then

$$|||\boldsymbol{u} - \boldsymbol{v}|||_* \leq \mathcal{M}(q, \boldsymbol{v}, f) =: \mathcal{M}_{\boldsymbol{u}}^{\oplus} \qquad \forall q \in Q_h^g. \tag{36}$$

The proof follows the abstract functional framework of [20, 34, 35] adapted to the non-matching mD setting: we expand the energy norm of the error using the weak primal form, apply the mD integration-by-parts formula of [1] on the admissible pair $(p - q, \boldsymbol{v}) \in H_0^1(\Omega) \times \mathbf{X}_{h,\mathrm{LC}}(f)$, and split each continuous transfer operator into its discrete realization plus a grid-mismatch defect. Cellwise Cauchy–Schwarz and the Poincaré–Wirtinger inequality (the latter applicable thanks to the local mass-conservation property of $\boldsymbol{v} \in \mathbf{X}_{h,\mathrm{LC}}(f)$ together with the cellwise mass-defect property of the discrete grid-mismatch operators) then yield the four global indicators in (32). For completeness, the full proof is given in Appendix A.

Remark 9 *(Nature of the estimates)* The majorant of Theorem 1 consists of two qualitatively different parts. The terms $\eta_{\mathrm{NM,DF}_\parallel,K}$, $\eta_{\mathrm{NM,DF}_\perp,K}$, and $\eta_{\mathrm{NM,R},K}$ are the diffusive and residual contributions obtained from the admissible pair after non-matching transfer and mimic the error indicators from [20] in structure. The additional terms $\eta_{\mathrm{GM,DF}_\parallel,K}$, $\eta_{\mathrm{GM,DF}_\perp,K}$, and $\eta_{\mathrm{GM,R},K}$ quantify the discrepancy introduced by evaluating the estimator on geometrically incompatible neighboring grids.

Remark 10 *(Behavior of grid mismatch indicators at lowest order)* For dual approximations with $k = 0$, the bulk grid-mismatch indicator $\eta_{\mathrm{GM,DF}_\parallel,K}$ and the higher-dimensional contribution to $\eta_{\mathrm{GM,R},K}$ vanish identically, since at $k = 0$ the constrained L^2 projection $\widetilde{\mathcal{D}}_{j,\hat{j}}^{\hat{j}}$ is the cell average and $\delta\mathcal{D}_j^{\hat{j}} v_j$ has zero face mean on every face of $\mathcal{T}_{\partial_j\Omega_{\hat{j}}}$. The interface mismatch $\eta_{\mathrm{GM,DF}_\perp,K}$ and the lower-dimensional contribution to $\eta_{\mathrm{GM,R},K}$ remain nontrivial, since they capture the loss of higher moments by the Scott–Zhang projection on Γ_j and by the constrained L^2 projection on $\mathcal{T}_{\Omega_j}$, respectively.

Corollary 1 *(Sharpness under grid compatibility) In the case when the mixed-dimensional grid is matching, $\mathcal{P}_\bullet^j = \widetilde{\mathcal{P}}_\bullet^j$ and $\mathcal{D}_j^\bullet = \widetilde{\mathcal{D}}_j^\bullet$, which implies zero defect and consequently $\eta_{\mathrm{GM,R},K} = \eta_{\mathrm{GM,DF}_\parallel,K} = \eta_{\mathrm{GM,DF}_\perp,K} = 0$. In this case, the majorant reduces to its standard form $\mathcal{M}(q, \boldsymbol{v}, f) = \eta_{\mathrm{DF}}(q, \boldsymbol{v}) + \eta_{\mathrm{R}}(\boldsymbol{v}, f)$ which matches with the error bounds for locally-mass conservative approximations on matching grids from [20, Sec. 5.2.3].*

Corollary 1 justifies the claim that the present work is an extension of our previous results [20] on matching grids.

5.3 Error indicators

It is often desirable to associate error estimates with an entire subdomain or interface grid. To this aim, we introduce the subdomain- and interface-level non-matching and

grid-mismatch error indicators

$$\eta^2_{\mathrm{NM},\Omega_i} := \sum_{K\in\mathcal{T}_{\Omega_i}} \left(\eta^2_{\mathrm{NM},\mathrm{DF}_\parallel,K} + \eta^2_{\mathrm{NM},\mathrm{R},K}\right), \quad \eta^2_{\mathrm{NM},\Gamma_j} := \sum_{K\in\mathcal{T}_{\Gamma_j}} \eta^2_{\mathrm{NM},\mathrm{DF}_\perp,K}, \tag{37}$$

$$\eta^2_{\mathrm{GM},\Omega_i} := \sum_{K\in\mathcal{T}_{\Omega_i}} \left(\eta^2_{\mathrm{GM},\mathrm{DF}_\parallel,K} + \eta^2_{\mathrm{GM},\mathrm{R},K}\right), \quad \eta^2_{\mathrm{GM},\Gamma_j} := \sum_{K\in\mathcal{T}_{\Gamma_j}} \eta^2_{\mathrm{GM},\mathrm{DF}_\perp,K}. \tag{38}$$

The total indicators associated with each subdomain and interface are

$$\eta^2_{\Omega_i} := \eta^2_{\mathrm{NM},\Omega_i} + \eta^2_{\mathrm{GM},\Omega_i}, \qquad \eta^2_{\Gamma_j} := \eta^2_{\mathrm{NM},\Gamma_j} + \eta^2_{\mathrm{GM},\Gamma_j}. \tag{39}$$

To report results for complex fracture networks, it is beneficial to aggregate subdomain and interface errors of the same dimensionality. Let $I_{d_i} \subseteq I$ and $J_{d_j} \subseteq J$ be the index sets of subdomains and interfaces of dimensions d_i and d_j, respectively. We then use

$$\eta^2_{\Omega^{d_i}} := \sum_{i\in I_{d_i}} \eta^2_{\Omega_i}, \qquad \eta^2_{\Gamma^{d_j}} := \sum_{j\in J_{d_j}} \eta^2_{\Gamma_j}, \tag{40}$$

to denote the indicators associated with all d_i-dimensional subdomains and all d_j-dimensional interfaces, respectively.

6 Computable estimates

Theorem 1 is independent of a particular numerical method, provided that the admissible pair belongs to $Q_h^g \times \mathbf{X}_{h,\mathrm{LC}}(f)$. We now describe two concrete realizations, based on the primal and dual weak forms from Sect. 3.3.

6.1 Primal and dual approximations

With the discrete projection operators formally defined, we can now write the approximated primal weak and dual problems. To this aim, consider first the mD broken space of polynomials on subdomains of order k or less:

$$\mathbb{P}_k(\mathcal{T}_\Omega) := \prod_{i\in I} \mathbb{P}_k(\mathcal{T}_{\Omega_i}). \tag{41}$$

Problem 5 (Approximated weak primal form on non-matching grids) *Let $k \geq 1$ be fixed and $p_h = [p_{h,i}]$, $g = [g_i] \in H^1(\Omega)$. Then, given $f = [f_i] \in L^2(\Omega)$, find $p_h \in \mathbb{P}_k(\mathcal{T}_\Omega) \cap (H^1_0(\Omega) + g)$ such that*

$$\begin{aligned}\sum_{i\in I}\sum_{K\in\mathcal{T}_{\Omega_i}} \left(\mathcal{K}_i\nabla_i p_{h,i}, \nabla_i q_{h,i}\right)_K + \sum_{j\in J}\sum_{K\in\mathcal{T}_{\Gamma_j}} \left(\kappa_j(\widetilde{\mathcal{P}}^j_{\check{j}} p_{h,\check{j}} - \widetilde{\mathcal{P}}^j_{\hat{j}} p_{h,\hat{j}}), \widetilde{\mathcal{P}}^j_{\check{j}} q_{h,\check{j}} - \widetilde{\mathcal{P}}^j_{\hat{j}} q_{h,\hat{j}}\right)_K \\ = \sum_{i\in I}\sum_{K\in\mathcal{T}_{\Omega_i}} \left(f_i, q_{h,i}\right)_K \qquad \forall q_h = [q_{h,i}] \in \mathbb{P}_k(\mathcal{T}_\Omega) \cap H^1_0(\Omega).\end{aligned} \tag{42}$$

Consider now the dual approximated problem. We wish to construct the discrete space for the mD fluxes, i.e., the discrete counterpart of $\mathbf{X}$. To this aim, we first consider the local Raviart-Thomas space given by

$$\mathbb{RT}_k(\mathcal{T}_{\Omega_i}) = \{\boldsymbol{v}_{h,i} \in \mathbf{H}(\mathrm{div}, \Omega_i) : \boldsymbol{v}_{h,i}|_K \in \mathbb{RT}_k(K) \ \forall\ K \in \mathcal{T}_{\Omega_i}\}. \tag{43}$$

Then, the space $\mathbf{X}_k$ is given by

$$\mathbf{X}_k = \prod_{i\in I}\left[\left(\mathbb{RT}_k(\mathcal{T}_{\Omega_i}) \cap \mathbf{V}_{0,i}\right) \times \prod_{j\in\check{S}_i} \widetilde{\mathcal{R}}_j^* \circ \widetilde{\mathcal{D}}_j^{\hat{j}}\, \mathbb{P}_k(\mathcal{T}_{\Gamma_j})\right], \tag{44}$$

where $\widetilde{\mathcal{R}}_j^* : \mathbb{P}_k(\mathcal{T}_{\partial_j\Omega_{\hat{j}}}) \to \mathbb{RT}_k(\mathcal{T}_{\Omega_{\hat{j}}})$ is the discrete extension operator from internal boundary grids onto the interior of higher-dimensional subdomain grids, cf. [13, 24] for a detailed discussion of the construction of this operator. We can now write the approximated dual weak problem as follows.

Problem 6 (Approximated weak dual form on non-matching grids) *Let $k \geq 0$ and $\boldsymbol{u}_h = [\boldsymbol{u}_{h,0,i}, \lambda_{h,j}]$, $p_h = [p_{h,i}]$. Then, given $f = [f_i] \in L^2(\Omega)$ and $g_D = [g_{D,i}] \in H^{1/2}(\partial_D\Omega)$, find $\boldsymbol{u}_h \in \mathbf{X}_k$ and $p_h \in \mathbb{P}_k(\mathcal{T}_\Omega)$ such that*

$$\begin{aligned}
&\sum_{i\in I}\sum_{K\in\mathcal{T}_{\Omega_i}} \left(\mathcal{K}_i^{-1}\left(\boldsymbol{u}_{h,0,i} + \textstyle\sum_{j\in\check{S}_i} \widetilde{\mathcal{R}}_j^* \circ \widetilde{\mathcal{D}}_j^{\hat{j}}\lambda_{h,j}\right), \boldsymbol{v}_{h,0,i} + \textstyle\sum_{j\in\check{S}_i} \widetilde{\mathcal{R}}_j^* \circ \widetilde{\mathcal{D}}_j^{\hat{j}} v_{h,j}\right)_K \\
&\quad - \sum_{i\in I}\sum_{K\in\mathcal{T}_{\Omega_i}} \left(p_{h,i}, \nabla_i \cdot \left(\boldsymbol{v}_{h,0,i} + \textstyle\sum_{j\in\check{S}_i} \widetilde{\mathcal{R}}_j^* \circ \widetilde{\mathcal{D}}_j^{\hat{j}} v_{h,j}\right) + \textstyle\sum_{j\in\hat{S}_i} \widetilde{\mathcal{D}}_j^{\check{j}} v_{h,j}\right)_K \\
&\quad + \sum_{j\in J}\sum_{K\in\mathcal{T}_{\Gamma_j}} \left(\kappa_j^{-1}\lambda_{h,j}, v_{h,j}\right)_K \\
&= -\sum_{i\in I}\sum_{K\in\mathcal{T}_{\partial_D\Omega_i}} \left(g_{D,i}, \left(\boldsymbol{v}_{h,0,i}\cdot\boldsymbol{n}_i\right)|_K\right)_K \qquad \forall \boldsymbol{v}_h = [\boldsymbol{v}_{h,0,i}, v_{h,j}] \in \mathbf{X}_k. \qquad (45a)\\
&\sum_{i\in I}\sum_{K\in\mathcal{T}_{\Omega_i}} \left(\nabla_i \cdot \left(\boldsymbol{u}_{h,0,i} + \textstyle\sum_{j\in\check{S}_i} \widetilde{\mathcal{R}}_j^* \circ \widetilde{\mathcal{D}}_j^{\hat{j}}\lambda_{h,j}\right), q_{h,i}\right)_K \\
&\quad - \sum_{i\in I}\sum_{K\in\mathcal{T}_{\Omega_i}} \left(\textstyle\sum_{j\in\hat{S}_i} \widetilde{\mathcal{D}}_j^{\check{j}}\lambda_{h,j}, q_{h,i}\right)_K \\
&= \sum_{i\in I}\sum_{K\in\mathcal{T}_{\Omega_i}} \left(f_i, q_{h,i}\right)_K \qquad \forall q_h = [q_{h,i}] \in \mathbb{P}_k(\mathcal{T}_\Omega). \qquad (45b)
\end{aligned}$$

In Problem 6, the Dirichlet boundary grid $\mathcal{T}_{\partial_D\Omega_i}$ is defined in analogy to (4.1).

Remark 11 *(Stability and relative refinement of interface grids)* It is well known that classical mortar methods require $\mathcal{T}_{\Gamma_j}$ to be coarser or equal than $\mathcal{T}_{\partial_j\Omega_{\hat{j}}}$. As shown in

[9], the introduction of a diffusive problem in the fractures guarantees uniqueness of the solution even when this is not the case. Nevertheless, as pointed out in [24], to avoid possible oscillations in the interface flux variable $\lambda_{h,j}$, it is desirable to adopt $\mathcal{T}_{\Gamma_j}$ coarser or equal than $\mathcal{T}_{\partial_j \Omega_{\hat{j}}}$ in practice.

6.2 Conforming fluxes and potentials

In order to apply the *a posteriori* bounds from Theorem 1, we need an mD potential in Q_h^g and an mD flux in $\mathbf{X}_{h,\mathrm{LC}}(f)$. Problem 5 only provides the first ingredient, whereas Problem 6 only provides the second ingredient. Thus, to obtain computable bounds using the finite element method one has to reconstruct the associated fluxes, while the mixed-finite element requires the reconstruction of potentials. Deriving optimal reconstruction techniques, even in the lowest-order case, is non-trivial, as one has to balance accuracy with computational cost. We therefore maintain the definition of conforming fluxes and potentials as general as possible while providing references to guide the reader.

Definition 9 *(Conforming flux)* We define a conforming flux as any function $\boldsymbol{\sigma}_h$ that satisfies

$$\boldsymbol{\sigma}_h \in \mathbf{X}_{h,\mathrm{LC}}(f). \tag{46}$$

Remark 12 *(On flux reconstruction)* Classical flux reconstruction techniques include (i) *superconvergent patch recovery* [36, 37] with $H(\mathrm{div})$-projections, (ii) local Neumann-patch solves [38–41], and (iii) hybrid explicit-recovery approaches [42]. In the mD setting, flux equilibration has been limited to enforcing mass balance across 2D/1D matrix–fracture interfaces couplings [17, 18, 43]. To our knowledge, a general mD flux reconstruction framework has not yet been proposed.

Definition 10 *(Conforming potential)* We define a conforming potential as any function s_h that satisfies

$$s_h \in Q_h^g. \tag{47}$$

Remark 13 *(On potential reconstruction)* Several techniques exist to recover continuous potentials from a non-conforming discretization in individual subdomains. Common approaches include: (i) patch-wise weighted average of cell-centered potentials (e.g., Green-Gauss, distance-weighted averages and least squares fits) [44–48], (ii) element-wise quadratic reconstruction via local polynomial solves [49, 50], and (iii) element-wise linear postprocessing based on lowest-order Raviart-Thomas basis functions [51]. Since the mD formulation does not require inter-dimensional continuity of potentials, any of these methods can be applied independently to each subdomain grid.

6.3 Fully computable a posteriori error estimates

Computable estimates are now readily available for primal and dual approximations.

Definition 11 *(Computable bounds for finite element approximations)* Let $p_h \in \mathbb{P}_k(\mathcal{T}_\Omega) \cap (H^1_0(\Omega) + g)$ with $k \geq 1$ be the solution to Problem 5, and $\boldsymbol{\sigma}_h \in \mathbf{X}_{h,\mathrm{LC}}(f)$ for $k \geq 0$ be a conforming flux in the sense of Definition 9. Then, set $q = p_h$ and $\boldsymbol{v} = \boldsymbol{\sigma}_h$ in Theorem 1 to obtain fully computable bounds.

Definition 12 *(Computable bounds for mixed-finite element approximations)* Let $(\boldsymbol{u}_h, p_h) \in \mathbf{X}_k \times \mathbb{P}_k(\mathcal{T}_\Omega)$ with $k \geq 0$ be the solution to Problem 6, and let $s_h \in \mathbb{P}_k(\mathcal{T}_\Omega) \cap (H^1_0(\Omega) + g)$ for $k \geq 1$ be a conforming potential in the sense of Definition 10. Then, set $q = s_h$ and $\boldsymbol{v} = \boldsymbol{u}_h$ in Theorem 1 to obtain fully computable bounds.

Thanks to the functional-based construction of the bounds in Theorem 1 and provided that approximate potentials and fluxes are properly reconstructed, other classical discretization techniques also fall within our framework. Important methods used in flow modeling in fractured porous media include the cell-centered finite volume method (CCFVM) [52, 53]—both the two-point flux approximation (TPFA) and the multi-point flux approximation (MPFA)—, the Vertex-Centered Finite Volume Method [54], the Mimetic Finite Difference Method [55, 56], the Discontinuous Galerkin Method [57, 58], and the Dual Mixed Virtual Element Method (MVEM) [12].

6.4 Effectivity indices

To quantify the efficiency of the *a posteriori* error estimates, we shall employ the following effectivity indices

$$I_p^{\mathrm{eff}} = \frac{\mathcal{M}_p^{\oplus}(s_h, \boldsymbol{\sigma}_h, f)}{|||p - s_h|||}, \qquad I_{\boldsymbol{u}}^{\mathrm{eff}} = \frac{\mathcal{M}_{\boldsymbol{u}}^{\oplus}(s_h, \boldsymbol{\sigma}_h, f)}{|||\boldsymbol{u} - \boldsymbol{\sigma}_h|||_*}. \tag{48}$$

7 Numerical examples

In this section, we present numerical verifications of the proposed non-matching error estimators against manufactured solutions and their application for test cases based on community benchmarks of flow in fractured porous media. For the sake of compactness, we only perform our analysis on mD domains with 3D hosts given that cases with 2D hosts are considerably less complex.

To obtain the numerical approximations, we employ the MPFA method [25, 52, 53], which is closely related to the lowest-order mixed-finite element approximation [59]. Fully computable estimates are obtained after two postprocessing steps:

(i) MPFA face fluxes are directly mapped to the coefficients of the local RT0 space (guaranteeing continuity of normal traces) [44]. Repeating this process in each subdomain grid yields a conforming mD flux $\boldsymbol{\sigma}_h \in \mathbf{X}_0$ (cf. Definition 9).

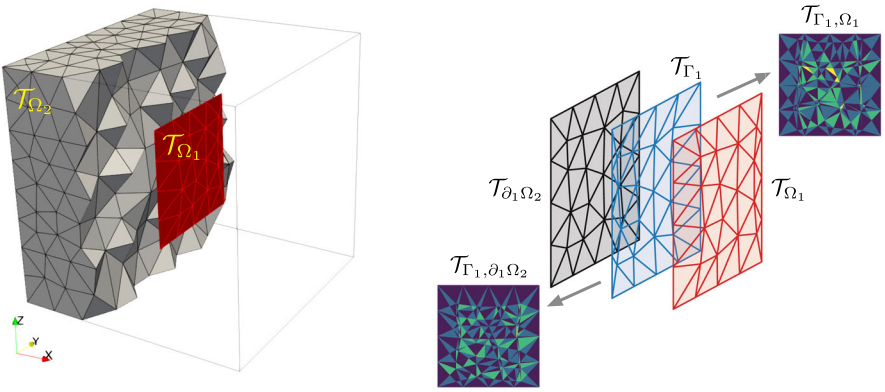


Fig. 5 3D/2D numerical verification setup. Left: Mixed-dimensional grid showcasing the matrix grid $\mathcal{T}_{\Omega_2}$ and the fully embedded fracture grid $\mathcal{T}_{\Omega_1}$. Right: Exploded view of the non-matching coupling between $\mathcal{T}_{\partial_1\Omega_2}$ (black), $\mathcal{T}_{\Gamma_1}$ (blue), and $\mathcal{T}_{\Omega_1}$ (red) with the corresponding transfer grids $\mathcal{T}_{\Gamma_1,\partial_1\Omega_2}$ and $\mathcal{T}_{\Gamma_1,\Omega_1}$ (triangles are colored for visualization purposes only). Example shown for $h = 0.15$ and translation $+\boldsymbol{e}_y$

(ii) MPFA potentials are reconstructed in each subdomain grid to obtain a conforming mD potential $s_h \in \mathbb{P}_1(\mathcal{T}_\Omega) \cap (H_0^1(\Omega) + g)$ using the potential reconstruction technique proposed in [51]. The technique employs the local MPFA face fluxes to first approximate a cell-centered potential gradient at the cell's barycenter which is then mapped to the cell vertices and added to the cell-center potential. This process produces $\mathbb{P}_1$-nodal potentials which are generally non-conforming. Thus, the Oswald interpolator is applied as a final step to produce a conforming global linear potential $s_h \in H_0^1(\Omega) + g$ (cf. Definition 10).

All numerical examples were implemented in `PorePy` [25] and are available for reproduction through the extension package `mdnme` [60].

7.1 3D/2D verification with a manufactured solution

We employ the 3D/2D manufactured solution from Section 7 of [20] to verify the efficiency of the proposed error estimators. The mD domain consists of a unit cube $\Omega_2 = (0, 1)^3$ hosting a fully embedded vertical fracture

$$\Omega_1 = \{(x, y, z) \in \mathbb{R}^3 : \ x = 0.5, \ 0.25 \leq y \leq 0.75, \ 0.25 \leq z \leq 0.75\}.$$

Interfaces Γ_1 and Γ_2 couple Ω_2 to the left and right sides of Ω_1, respectively (see Fig. 5). With a smooth matrix pressure $p_2 : \Omega_2 \to \mathbb{R}$, unit tangential permeabilities $\mathcal{K}_2 = \mathbf{I}_{3\times3}$ and $\mathcal{K}_1 = \mathbf{I}_{2\times2}$, the exact Darcy fluxes $\boldsymbol{u}_2 : \Omega_2 \to \mathbb{R}^3$ and $\boldsymbol{u}_1 : \Omega_1 \to \mathbb{R}^2$ follow from (2b). With unit normal permeabilities $\kappa_1 = \kappa_2 = 1$, the interface fluxes $\lambda_1 : \Gamma_1 \to \mathbb{R}$ and $\lambda_2 : \Gamma_2 \to \mathbb{R}$ follow from (2c). Finally, (2a) gives the exact sources $f_2 : \Omega_2 \to \mathbb{R}$ and $f_1 : \Omega_1 \to \mathbb{R}$. Exact expressions are listed in Appendix D.2 of [20].

We consider four refinement levels with target mesh sizes $h \in \{0.3, 0.15, 0.075, 0.0375\}$. For each h, we first build a fully matching tessellation of the mD grid (ref-

erence configuration). From this, we generate non-matching grids by systematically perturbing internal nodes of the fracture grid $\mathcal{T}_{\Omega_1}$ and the interface side grids $\mathcal{T}_{\Gamma_1}$ and $\mathcal{T}_{\Gamma_2}$. Concretely, each internal node of $\mathcal{T}_{\Omega_1}$ is translated by half of the grid's mean cell diameter in the eight in-plane directions $\{\pm\boldsymbol{e}_y, \pm\boldsymbol{e}_z, \pm(\boldsymbol{e}_y + \boldsymbol{e}_z), \pm(\boldsymbol{e}_y - \boldsymbol{e}_z)\}$, while internal nodes of $\mathcal{T}_{\Gamma_1}$ and $\mathcal{T}_{\Gamma_2}$ are perturbed in the opposite directions (same magnitude). Nodes of the internal boundary grids $\mathcal{T}_{\partial_1\Omega_2}$ and $\mathcal{T}_{\partial_2\Omega_2}$ are left unperturbed. This procedure yields eight fully non-matching configurations per h; see the right panel of Fig. 5 for the left non-matching coupling corresponding to $h = 0.15$ and $+\boldsymbol{e}_y$ perturbation direction.

Table 1 reports the subdomain and interface-wise non-matching and grid-mismatch error indicators together with the majorants, true errors, and effectivity indices for both matching (M) and non-matching (NM) realizations. For the non-matching results we report the mean over the eight perturbations together with the sample standard deviation. The results indicate that: (i) grid mismatch terms are about one order of magnitude smaller than their corresponding non-matching terms, (ii) majorants and effectivity indices for the primal and dual variables remain close to the matching baseline, and (iii) subdomain and interface contributions decrease monotonically with refinement. Moreover, as indicated in Remark 10, $\eta_{\mathrm{GM},\mathrm{DF}_\parallel,K}$ is exactly zero (up to machine precision) and therefore not included in the table. It is worth emphasizing that the tested non-matching couplings used in this example are deliberately challenging (fully non-matching with finite perturbations) to stress-test the estimators; in applications, controlled refinement typically leads to even milder mismatches.

As can be verified in Table 1, the errors associated to the bulk subdomain Ω_2 are dominant in all realizations. To show the potential of disjoint adaptivity guided by the error indicators, we complement the previous test with an additional experiment. In this experiment, we identify the subdomain with the highest error and uniformly refine it (via simplex bisection [61]) while keeping all the other grids fixed. During this process, non-matching grids are produced. The results are shown in Table 2 for four refinement steps. We can see that the error in the bulk monotonically decreases with refinement. However, due to the highly non-matching coupling, errors for the fracture and interfaces do not show a consistent decrease. Nevertheless, the estimators remain reliable for both pressure and flux variables as can be verified from the efficiency indices.

7.2 Regular fracture network

This numerical example employs the setup of Case 2: Regular network, from the 3D flow benchmark [7]. The mD domain consists of a unit cube matrix hosting nine regularly oriented fractures (see the left panel of Fig. 6), resulting in an mD domain with one 3D subdomain, nine 2D subdomains, sixty-nine 1D subdomains, and twenty-seven 0D intersection points.

The original benchmark prescribes no-flux boundary conditions in all external faces except on the red and blue regions, where a constant Darcy flux ($\boldsymbol{u} = -1$) and a constant pressure ($p = 1$) are imposed, respectively. Since our theory does not cover non-zero external boundary fluxes, and following [20], we replace the inflow Neumann

Table 1 Verification of the 3D/2D manufactured solution

	$h = 0.3$		$h = 0.15$		$h = 0.075$		$h = 0.0375$	
	M	NM	M	NM	M	NM	M	NM
$\eta_{\mathrm{NM},\Omega_2}$	2.49e−01	2.49e−01 ± 1.61e−04	1.77e−01	1.77e−01 ± 1.39e−04	9.21e−02	9.20e−02 ± 7.44e−05	4.79e−02	4.80e−02 ± 4.09e−05
$\eta_{\mathrm{NM},\Omega_1}$	8.56e−03	5.71e−03 ± 6.09e−03	1.63e−05	3.28e−03 ± 3.49e−03	2.92e−03	1.81e−03 ± 1.92e−03	5.31e−06	8.77e−04 ± 9.34e−04
$\eta_{\mathrm{NM},\Gamma_1}$	7.04e−03	2.74e−02 ± 8.05e−03	2.29e−03	2.41e−02 ± 3.31e−03	4.69e−04	4.25e−03 ± 1.06e−03	7.94e−05	2.63e−03 ± 1.25e−03
$\eta_{\mathrm{NM},\Gamma_2}$	5.56e−03	2.23e−02 ± 2.38e−03	2.46e−03	2.46e−02 ± 3.37e−03	4.61e−04	4.20e−03 ± 1.08e−03	8.08e−05	2.61e−03 ± 1.29e−03
$\eta_{\mathrm{GM},\Gamma_1}$	–	2.59e−03 ± 4.35e−04	–	8.13e−04 ± 1.26e−04	–	7.86e−05 ± 7.14e−06	–	1.81e−05 ± 3.27e−06
$\eta_{\mathrm{GM},\Gamma_2}$	–	1.21e−03 ± 2.51e−04	–	8.54e−04 ± 1.21e−04	–	8.21e−05 ± 9.12e−06	–	1.77e−05 ± 3.05e−06
$\eta_{\mathrm{GM},\Omega_1}$	–	4.37e−05 ± 1.66e−05	–	1.43e−05 ± 1.14e−05	–	4.03e−06 ± 3.94e−06	–	9.60e−07 ± 1.02e−06
$\mathcal{M}_p^{\oplus} = \mathcal{M}_{\boldsymbol{u}}^{\oplus}$	2.75e−01	2.77e−01 ± 1.56e−03	1.93e−01	1.97e−01 ± 1.18e−03	9.66e−02	9.68e−02 ± 2.84e−04	4.92e−02	4.94e−02 ± 2.10e−04
$\lvert\!\lvert\!\lvert p - p_h \rvert\!\rvert\!\rvert$	2.40e−01	2.43e−01 ± 7.76e−04	1.71e−01	1.75e−01 ± 4.50e−04	8.85e−02	8.82e−02 ± 4.86e−04	4.55e−02	4.64e−02 ± 8.82e−04
$\lvert\!\lvert\!\lvert \boldsymbol{u} - \boldsymbol{\sigma}_h \rvert\!\rvert\!\rvert_*$	7.20e−02	7.16e−02 ± 4.17e−04	4.94e−02	5.01e−02 ± 7.14e−04	3.16e−02	3.05e−02 ± 1.26e−03	1.54e−02	1.75e−02 ± 2.23e−03
I_p^{eff}	1.15e+00	1.14e+00 ± 6.94e−03	1.13e+00	1.13e+00 ± 5.16e−03	1.09e+00	1.10e+00 ± 3.01e−03	1.08e+00	1.07e+00 ± 1.58e−02
$I_{\boldsymbol{u}}^{\mathrm{eff}}$	3.82e+00	3.88e+00 ± 1.75e−02	3.91e+00	3.93e+00 ± 4.95e−02	3.05e+00	3.18e+00 ± 1.23e−01	3.19e+00	2.87e+00 ± 3.53e−01

Subdomain and interface error indicators, global majorants $\mathcal{M}_p^{\oplus} = \mathcal{M}_{\boldsymbol{u}}^{\oplus}$, true errors in pressure and flux, and effectivity indices. Column M: single matching-grid run; column NM: mean ± std over 8 mortar-translation directions

Table 2 Guided subdomain halving for the 3D/2D benchmark

Step	$\lvert\mathcal{T}_{\Omega_2}\rvert$	$\lvert\mathcal{T}_{\Omega_1}\rvert$	η_{Ω^3}	η_{Ω^2}	η_{Γ^2}	$\mathcal{M}_p^{\oplus} = \mathcal{M}_{\boldsymbol{u}}^{\oplus}$	$I_{\text{eff},p}$	$I_{\text{eff},\boldsymbol{u}}$
0	941	14	2.56e−01	5.23e−05	1.10e−02	2.83e−01	1.145	3.826
1	7,528	14	1.43e−01	2.42e−05	1.54e−02	1.52e−01	1.098	3.723
2	60,224	14	7.25e−02	2.97e−05	2.22e−04	7.46e−02	1.072	3.576
3	481,792	14	3.64e−02	3.11e−05	8.77e−04	3.70e−02	1.058	3.539

At each step the subdomain with the larger indicator (η_{Ω^3} or η_{Ω^2}) is bisected independently while the other remains fixed; the configuration is non-matching from step 1 onward. $\lvert\mathcal{T}_{\Omega_2}\rvert$ and $\lvert\mathcal{T}_{\Omega_1}\rvert$ denote the cell counts in the bulk and fracture subdomains, respectively

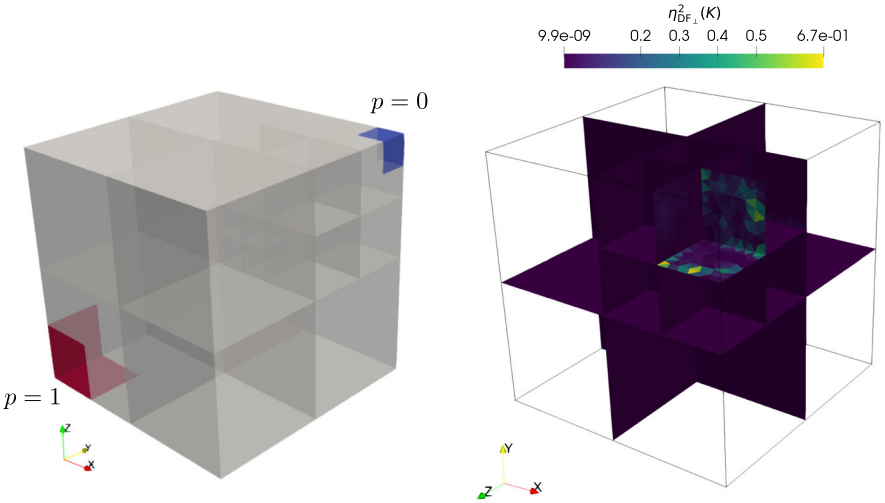


Fig. 6 Regular network. Left: Geometry of the fracture network and boundary conditions. Right: Local diffusive error estimators of 2D interface grids for the finest mesh resolution

condition by a Dirichlet condition with $p = 1$ and set the outlet pressure to $p = 0$. The matrix subdomain is assigned permeability values $\mathcal{K} \in \{1, 0.1\}$, while the fractures are considered conductive ($\mathcal{K} = 1 \times 10^4$). The complete set of parameters can be found in Table 4 from [7].

The benchmark employs three levels of refinement, with approximately 500, 1 400 and 32 000 three-dimensional cells. To generate the non-matching grids, we begin from a fully matching tessellation of the mD domain and then globally refine all fracture grids using nested bisection [61]. Importantly, we do not refine the 1D subdomains grids. Refining 1D subdomain grids increases the resolution around intersection points—well-known points of singularity—without improving the accuracy of interface fluxes, resulting in a larger mismatch between the interface fluxes and the (permeability-scaled) pressure jumps (2c). We emphasize that this phenomenon is related to the limited regularity of the model itself [3], rather than to any deficiency of the error estimators.

Table 3 Majorant and dimension-based aggregated error estimators for the 3D regular network benchmark from Sect. 7.2

Mesh	η_{Ω^3}	η_{Ω^2}	η_{Ω^1}	η_{Γ^2}	η_{Γ^1}	η_{Γ^0}	$\mathcal{M}_p^{\oplus} = \mathcal{M}_{\boldsymbol{u}}^{\oplus}$
Coarse	5.70e−01	1.39e−02	2.01e−04	1.98e+02	6.47e−01	1.15e−02	1.98e+02
Intermediate	3.84e−01	7.21e−03	1.25e−04	2.90e+01	1.96e+00	2.69e−03	2.90e+01
Fine	3.24e−01	4.04e−03	9.84e−05	6.53e+00	4.06e−01	1.90e−03	6.55e+00

Table 3 reports the aggregated local errors grouped by dimensionality, together with the majorant. All quantities (except for η_{Γ^1}) decrease monotonically with refinement. The dominant contributions to the majorant originate from the 2D interfaces, highlighting that MPFA struggles to accurately represent the interface law; this is expected considering that it is a lowest-order method. The right panel of Fig. 6 shows the spatial distribution of the local diffusive errors. Not surprisingly, the largest errors are located around the outlet boundary region, where steep pressure gradients occur.

7.3 Production on a fracture network with small features

In this numerical example, we consider the setup of Case 3: Network with small features from the 3D verification benchmark [7] to analyze non-matching approximations of an idealized injection/production scenario. To reduce the influence of boundary conditions on the error estimates, we modify the original specification (cf. Section 5.3 of [7]) and impose no-flux boundary conditions on all boundaries except the South and North sides, where we prescribe a constant Dirichlet condition $p = 0$; see the left panel of Fig. 7. We then add an injection well on Ω_2 and a production well on Ω_4, modeled as constant source terms on the well cells:

$$f_2(\mathbf{x}) = \begin{cases} 0.1, & \mathbf{x} = (0.5, 0.65, 0.5) \\ 0, & \text{elsewhere} \end{cases} \quad \text{and} \quad f_4(\mathbf{x}) = \begin{cases} -0.1, & \mathbf{x} = (0.5, 1.6, 0.675) \\ 0, & \text{elsewhere} \end{cases},$$

where the conditions on $\mathbf{x}$ imply the cell containing said coordinate. Following the benchmark, we assign unitary permeability in the matrix $\mathcal{K} = 1$ and $\mathcal{K} = 1 \times 10^4$ in the fractures, while the remaining material parameters are taken from Table 5 of [7]. The resulting pressure distribution is shown in the right panel of Fig. 7.

In contrast to the previous numerical example, our goal here is not to perform a full convergence study, but to compare matching and non-matching approximations. As before, the non-matching mD grid is constructed by bisecting the matching mD grid and replacing the finer fracture grids into the coarser mD grid.

Table 4 shows the aggregated error contributions for both discretizations. The non-matching estimators closely reproduce the matching ones, with differences at most a few percent and a relative deviation of approximately 1.6% in the majorant. The non-matching approximation yields slightly smaller contributions in all aggregated quantities except for η_{Γ^2}. This illustrates the subtlety of non-matching refinement in mD geometries: refining fractures without fully refining interfaces may reduce errors

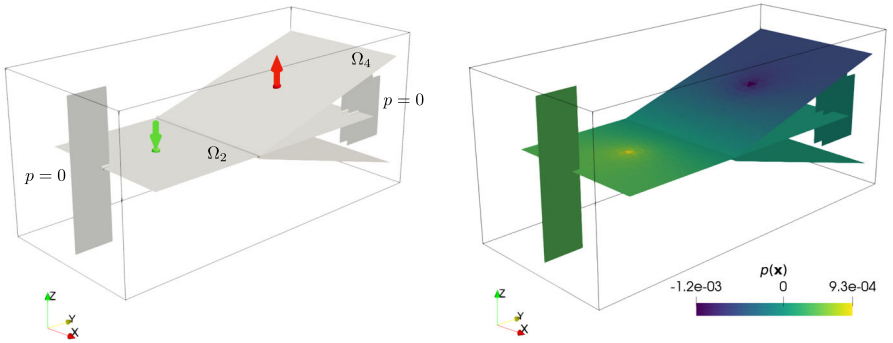


Fig. 7 Network with small features. Left: Geometry, boundary conditions, and source/sink locations. Right: Resulting pressure distribution (shown only on 2D subdomains for visualization)

Table 4 Majorant and dimension-based aggregated error estimators for the 3D fracture network with small features from Sect. 7.3

Approximation	η_{Ω^3}	η_{Ω^2}	η_{Ω^1}	η_{Γ^2}	η_{Γ^1}	$\mathcal{M}_p^{\oplus} = \mathcal{M}_{\boldsymbol{u}}^{\oplus}$
Matching	8.08e−04	5.72e−03	3.08e−06	1.22e−01	1.04e−04	1.22e−01
Non-matching	7.89e−04	5.71e−03	2.72e−06	1.24e−01	7.23e−05	1.24e−01

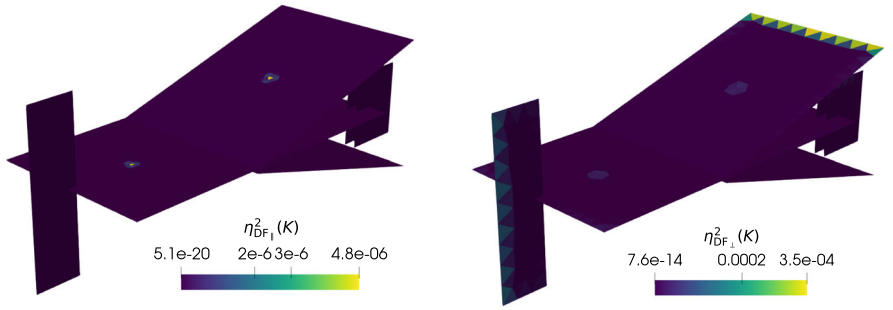


Fig. 8 Non-matching local error estimators for the 3D fracture network with small features. Left: 2D diffusive errors on subdomains. Right: 2D diffusive errors on interfaces

in some components while increasing them in others. Moreover, as pointed out in Remark 11, $\mathcal{T}_{\Gamma_j}$ cannot be refined freely without simultaneously refining $\mathcal{T}_{\partial_j \Omega_j}$, as this may violate inf-sup stability conditions [13, 24]. Finally, it is important to remark that the residual contributions vanish for both approximations due to the local mass-conservative properties of MPFA [20].

Figure 8 shows the spatial distribution of the 2D subdomain and interface non-matching diffusive errors for the non-matching approximation. As expected, the largest subdomain errors occur near the injection and production wells. In contrast, the interface errors are primarily concentrated along the fracture boundaries, which are known to be challenging regions for mD flow discretizations.

8 Conclusion

In this article, we have extended the *a posteriori* error estimators developed in [20] for matching grids to the setting of non-matching mD discretizations for elliptic problems, with particular emphasis on single-phase flow in fractured porous media. Using postprocessed MPFA approximations, we verified the validity of the proposed non-matching estimators—and, consequently, of the underlying discrete projection and grid mismatch operators—on synthetic test cases with exact solutions as well as on 3D community benchmark problems featuring complex geometries and realistic material-parameter contrasts. The results confirm that the estimators remain reliable under non-matching refinement, while simultaneously highlighting the delicate interplay between accuracy, refinement choices, and stability requirements in mD settings.

Appendix A Proof of Theorem 1

In this section, we provide a complete proof of Theorem 1.

A.1 Upper bound on the primal variable

Let $p = [p_i] \in H_0^1(\Omega) + g$ be the solution to primal weak form and let $q = [q_i] \in Q_h^g \subset (H_0^1(\Omega) + g)$ be an arbitrary potential. Define

$$e := [p_i - q_i] \in H_0^1(\Omega),$$

as the primal error. Thus,

$$\begin{aligned}
|||e|||^2 &= \sum_{i\in I} (\mathcal{K}_i \nabla_i (p_i - q_i), \nabla_i e_i)_{\Omega_i} \\
&\quad + \sum_{j\in J} \left(\kappa_j \left(\mathcal{P}_{\check{j}}^j (p_{\check{j}} - q_{\check{j}}) - \mathcal{P}_{\hat{j}}^j (p_{\hat{j}} - q_{\hat{j}})\right), \mathcal{P}_{\check{j}}^j e_{\check{j}} - \mathcal{P}_{\hat{j}}^j e_{\hat{j}}\right)_{\Gamma_j} \\
&= \sum_{i\in I} (\mathcal{K}_i \nabla_i p_i, \nabla_i (p_i - q_i))_{\Omega_i} + \sum_{i\in I} (-\mathcal{K}_i \nabla_i q_i, \nabla_i e_i)_{\Omega_i} \\
&\quad + \sum_{j\in J} \left(\kappa_j \left(\mathcal{P}_{\check{j}}^j p_{\check{j}} - \mathcal{P}_{\hat{j}}^j p_{\hat{j}}\right), \mathcal{P}_{\check{j}}^j e_{\check{j}} - \mathcal{P}_{\hat{j}}^j e_{\hat{j}}\right)_{\Gamma_j} \\
&\quad + \sum_{j\in J} \left(-\kappa_j \left(\mathcal{P}_{\check{j}}^j q_{\check{j}} - \mathcal{P}_{\hat{j}}^j q_{\hat{j}}\right), \mathcal{P}_{\check{j}}^j e_{\check{j}} - \mathcal{P}_{\hat{j}}^j e_{\hat{j}}\right)_{\Gamma_j}
\end{aligned} \tag{A1}$$

Since $e \in H_0^1(\Omega)$, it may be used as a test function in the weak primal formulation. Hence, the sum of the first and third terms of (A1) coincides with the right-hand side of the weak primal form (Problem 3). We can therefore write the equality

$$|||e|||^2 = \sum_{i\in I} (f_i, e_i)_{\Omega_i} + \sum_{i\in I} (-\mathcal{K}_i \nabla_i q_i, \nabla_i e_i)_{\Omega_i}$$

$$+\sum_{j\in J}\left(-\kappa_j\left(\mathcal{P}_{\check{j}}^{j}q_{\check{j}}-\mathcal{P}_{\hat{j}}^{j}q_{\hat{j}}\right),\mathcal{P}_{\check{j}}^{j}e_{\check{j}}-\mathcal{P}_{\hat{j}}^{j}e_{\hat{j}}\right)_{\Gamma_j}. \tag{A2}$$

Let us now fix any $\boldsymbol{v}=[\boldsymbol{v}_{0,i},v_j]\in\mathbf{X}_{h,\mathrm{LC}}(f)$ and use the mixed-dimensional integration-by-parts formula [1, 20] on the pair $(e,\boldsymbol{v})\in H_0^1(\Omega)\times\mathbf{X}_{h,\mathrm{LC}}(f)$ (the embedding $\mathbf{X}_{h,\mathrm{LC}}(f)\subset\mathbf{X}$ allows to invoke the mD integration by parts on continuous data) to construct the identity:

$$\begin{aligned}
&-\sum_{i\in I}\left(\nabla_i\cdot\left(\boldsymbol{v}_{0,i}+\textstyle\sum_{j\in\check{S}_i}\mathcal{R}_j^*\circ\mathcal{D}_j^{\hat{j}}v_j\right)-\sum_{j\in\hat{S}_i}\mathcal{D}_j^{\check{j}}v_j,e_i\right)_{\Omega_i}\\
&-\sum_{i\in I}\left(\boldsymbol{v}_{0,i}+\textstyle\sum_{j\in\check{S}_i}\mathcal{R}_j^*\circ\mathcal{D}_j^{\hat{j}}v_j,\nabla_i e_i\right)_{\Omega_i}-\sum_{j\in J}\left(v_j,\mathcal{P}_{\check{j}}^{j}e_{\check{j}}-\mathcal{P}_{\hat{j}}^{j}e_{\hat{j}}\right)_{\Gamma_j}=0.
\end{aligned} \tag{A3}$$

Adding (A3) to (A2), results in the following equality:

$$\begin{aligned}
|||e|||^2=&\sum_{i\in I}\left(f_i-\nabla_i\cdot\left(\boldsymbol{v}_{0,i}+\textstyle\sum_{j\in\check{S}_i}\mathcal{R}_j^*\circ\mathcal{D}_j^{\hat{j}}v_j\right)+\sum_{j\in\hat{S}_i}\mathcal{D}_j^{\check{j}}v_j,e_i\right)_{\Omega_i}\\
&+\sum_{i\in I}\left(-\left(\boldsymbol{v}_{0,i}+\textstyle\sum_{j\in\check{S}_i}\mathcal{R}_j^*\circ\mathcal{D}_j^{\hat{j}}v_j+\mathcal{K}_i\nabla_i q_i\right),\nabla_i e_i\right)_{\Omega_i}\\
&+\sum_{j\in J}\left(-\left(v_j+\kappa_j\left(\mathcal{P}_{\check{j}}^{j}q_{\check{j}}-\mathcal{P}_{\hat{j}}^{j}q_{\hat{j}}\right)\right),\mathcal{P}_{\check{j}}^{j}e_{\check{j}}-\mathcal{P}_{\hat{j}}^{j}e_{\hat{j}}\right)_{\Gamma_j}.
\end{aligned} \tag{A4}$$

Using the additive splittings between continuous transfer operators and their discrete realizations,

$$\begin{aligned}
\mathcal{D}_j^{\hat{j}}v_j&=\widetilde{\mathcal{D}}_j^{\hat{j}}v_j+\delta\mathcal{D}_j^{\hat{j}}v_j,\qquad \mathcal{D}_j^{\check{j}}v_j=\widetilde{\mathcal{D}}_j^{\check{j}}v_j+\delta\mathcal{D}_j^{\check{j}}v_j,\\
\mathcal{P}_{\hat{j}}^{j}q_{\hat{j}}&=\widetilde{\mathcal{P}}_{\hat{j}}^{j}q_{\hat{j}}+\delta\mathcal{P}_{\hat{j}}^{j}q_{\hat{j}},\qquad \mathcal{P}_{\check{j}}^{j}q_{\check{j}}=\widetilde{\mathcal{P}}_{\check{j}}^{j}q_{\check{j}}+\delta\mathcal{P}_{\check{j}}^{j}q_{\check{j}},
\end{aligned}$$

together with the convention that $\widetilde{\mathcal{R}}_j^*$ acts as the discrete realization of $\mathcal{R}_j^*$ on the matching internal-boundary–bulk coupling (cf. Sect. 4.2), the positive square roots of the positive definite factorization of $\mathcal{K}_i$ and κ_j, and the additivity of the subdomain and interface inner products over the corresponding non-matching grids, identity (A4) can be written as

$$\begin{aligned}
|||e|||^2=&\sum_{i\in I}\sum_{K\in\mathcal{T}_{\Omega_i}}\underbrace{\left(f_i-\nabla_i\cdot\left(\boldsymbol{v}_{0,i}+\textstyle\sum_{j\in\check{S}_i}\widetilde{\mathcal{R}}_j^*\circ\widetilde{\mathcal{D}}_j^{\hat{j}}v_j\right)+\sum_{j\in\hat{S}_i}\widetilde{\mathcal{D}}_j^{\check{j}}v_j,e_i\right)_K}_{T_1}\\
&+\sum_{i\in I}\sum_{K\in\mathcal{T}_{\Omega_i}}\underbrace{\left(-\mathcal{K}_i^{-1/2}\left(\boldsymbol{v}_{0,i}+\textstyle\sum_{j\in\check{S}_i}\widetilde{\mathcal{R}}_j^*\circ\widetilde{\mathcal{D}}_j^{\hat{j}}v_j+\mathcal{K}_i\nabla_i q_i\right),\mathcal{K}_i^{1/2}\nabla_i e_i\right)_K}_{T_2}\\
&+\sum_{j\in J}\sum_{K\in\mathcal{T}_{\Gamma_j}}\underbrace{\left(-\kappa_j^{-1/2}\left(v_j+\kappa_j\left(\widetilde{\mathcal{P}}_{\check{j}}^{j}q_{\check{j}}-\widetilde{\mathcal{P}}_{\hat{j}}^{j}q_{\hat{j}}\right)\right),\kappa_j^{1/2}(\mathcal{P}_{\check{j}}^{j}e_{\check{j}}-\mathcal{P}_{\hat{j}}^{j}e_{\hat{j}})\right)_K}_{T_3}
\end{aligned}$$

$$
\begin{aligned}
&+\sum_{i\in I}\sum_{K\in\mathcal{T}_{\Omega_i}} \underbrace{\left(\nabla_i\cdot\textstyle\sum_{j\in\check{\mathcal{S}}_i}\widetilde{\mathcal{R}}_j^{*}\circ\delta\mathcal{D}_j^{\hat{\jmath}}v_j+\sum_{j\in\hat{\mathcal{S}}_i}\delta\mathcal{D}_j^{\check{\jmath}}v_j,\,e_i\right)_K}_{T_4}\\
&+\sum_{i\in I}\sum_{K\in\mathcal{T}_{\Omega_i}} \underbrace{\left(-\mathcal{K}_i^{-1/2}\textstyle\sum_{j\in\check{\mathcal{S}}_i}\widetilde{\mathcal{R}}_j^{*}\circ\delta\mathcal{D}_j^{\hat{\jmath}}v_j,\,\mathcal{K}_i^{1/2}\nabla_i e_i\right)_K}_{T_5}\\
&+\sum_{j\in J}\sum_{K\in\mathcal{T}_{\Gamma_j}} \underbrace{\left(-\kappa_j^{-1/2}\left(\kappa_j\left(\delta\mathcal{P}_{\check{\jmath}}^{j}q_{\check{\jmath}}-\delta\mathcal{P}_{\hat{\jmath}}^{j}q_{\hat{\jmath}}\right)\right),\,\kappa_j^{1/2}(\mathcal{P}_{\check{\jmath}}^{j}e_{\check{\jmath}}-\mathcal{P}_{\hat{\jmath}}^{j}e_{\hat{\jmath}})\right)_K}_{T_6}.
\end{aligned}
\tag{A5}
$$

For the sake of compactness, in the following, we shall use

$$
\sum_{i,K}\bullet=\sum_{i\in I}\sum_{K\in\mathcal{T}_{\Omega_i}}\bullet,\qquad \sum_{j,K}\bullet=\sum_{j\in J}\sum_{K\in\mathcal{T}_{\Gamma_j}}\bullet. \tag{A6}
$$

We now bound each of the six terms cellwise.

Bound on T_1. The flux $\boldsymbol{v}\in\mathbf{X}_{h,\mathrm{LC}}(f)$ satisfies the local mass-conservation property $(\widetilde{r}_i,1)_K=0$ for every $K\in\mathcal{T}_{\Omega_i}$ (cf. Definition 7), where

$$
\widetilde{r}_i:=f_i-\nabla_i\bullet\left(\boldsymbol{v}_{0,i}+\textstyle\sum_{j\in\check{\mathcal{S}}_i}\widetilde{\mathcal{R}}_j^{*}\circ\widetilde{\mathcal{D}}_j^{\hat{\jmath}}v_j\right)+\sum_{j\in\hat{\mathcal{S}}_i}\widetilde{\mathcal{D}}_j^{\check{\jmath}}v_j
$$

denotes the discrete residual on K. Subtracting the cell mean $\overline{e_i}^K\in\mathbb{R}$ of e_i on K leaves the term unchanged, and the Poincaré–Wirtinger inequality on the convex simplex K together with the ellipticity bound $\|\nabla_i e_i\|_K\le c_{\mathcal{K}_i,K}^{-1}\left\|\mathcal{K}_i^{1/2}\nabla_i e_i\right\|_K$ from Assumption 2 yield

$$
\begin{aligned}
|T_1|&=\left|\left(\widetilde{r}_i,\,e_i-\overline{e_i}^K\right)_K\right|\le\|\widetilde{r}_i\|_K\cdot\frac{h_K}{\pi}\|\nabla_i e_i\|_K\\
&\le\frac{h_K}{\pi c_{\mathcal{K}_i,K}}\|\widetilde{r}_i\|_K\cdot\left\|\mathcal{K}_i^{1/2}\nabla_i e_i\right\|_K=\eta_{\mathrm{NM,R},K}\left\|\mathcal{K}_i^{1/2}\nabla_i e_i\right\|_K.
\end{aligned}
\tag{A7}
$$

Bound on T_4. Define the grid-mismatch residual

$$
\rho_i:=\nabla_i\cdot\textstyle\sum_{j\in\check{\mathcal{S}}_i}\widetilde{\mathcal{R}}_j^{*}\circ\delta\mathcal{D}_j^{\hat{\jmath}}v_j+\sum_{j\in\hat{\mathcal{S}}_i}\delta\mathcal{D}_j^{\check{\jmath}}v_j,
$$

so that $T_4=(\rho_i,e_i)_K$. By the cellwise mass-defect property of the discrete grid-mismatch operators (cf. Lemma 3), $(\rho_i,1)_K=0$ for every $K\in\mathcal{T}_{\Omega_i}$. The same Poincaré–Wirtinger argument as for T_1 then yields

$$
|T_4|\le\frac{h_K}{\pi c_{\mathcal{K}_i,K}}\|\rho_i\|_K\cdot\left\|\mathcal{K}_i^{1/2}\nabla_i e_i\right\|_K=\eta_{\mathrm{GM,R},K}\left\|\mathcal{K}_i^{1/2}\nabla_i e_i\right\|_K. \tag{A8}
$$

Bounds on T_2 and T_5. Direct application of the Cauchy–Schwarz inequality gives

$$\begin{aligned}|T_2| &\le \left\| \mathcal{K}_i^{-1/2}\Big(\boldsymbol{v}_{0,i} + \textstyle\sum_{j\in\check{\mathcal{S}}_i} \widetilde{\mathcal{R}}_j^{*} \circ \widetilde{\mathcal{D}}_j^{\hat{\jmath}} v_j\Big) + \mathcal{K}_i^{1/2}\nabla_i q_i \right\|_K \cdot \left\| \mathcal{K}_i^{1/2}\nabla_i e_i \right\|_K \\ &= \eta_{\mathrm{NM},\mathrm{DF}_\parallel,K} \left\| \mathcal{K}_i^{1/2}\nabla_i e_i \right\|_K, \qquad \text{(A9)}\\ |T_5| &\le \left\| \mathcal{K}_i^{-1/2} \textstyle\sum_{j\in\check{\mathcal{S}}_i} \widetilde{\mathcal{R}}_j^{*} \circ \delta\mathcal{D}_j^{\hat{\jmath}} v_j \right\|_K \cdot \left\| \mathcal{K}_i^{1/2}\nabla_i e_i \right\|_K = \eta_{\mathrm{GM},\mathrm{DF}_\parallel,K} \left\| \mathcal{K}_i^{1/2}\nabla_i e_i \right\|_K. \qquad \text{(A10)}\end{aligned}$$

Bounds on T_3 and T_6. Analogously, on each $K \in \mathcal{T}_{\Gamma_j}$,

$$\begin{aligned}|T_3| &\le \left\| \kappa_j^{-1/2} v_j + \kappa_j^{1/2}\big(\widetilde{\mathcal{P}}_{\check{\jmath}}^{j} q_{\check{\jmath}} - \widetilde{\mathcal{P}}_{\hat{\jmath}}^{j} q_{\hat{\jmath}}\big) \right\|_K \cdot \left\| \kappa_j^{1/2}\big(\mathcal{P}_{\check{\jmath}}^{j} e_{\check{\jmath}} - \mathcal{P}_{\hat{\jmath}}^{j} e_{\hat{\jmath}}\big) \right\|_K \\ &= \eta_{\mathrm{NM},\mathrm{DF}_\perp,K} \left\| \kappa_j^{1/2}\big(\mathcal{P}_{\check{\jmath}}^{j} e_{\check{\jmath}} - \mathcal{P}_{\hat{\jmath}}^{j} e_{\hat{\jmath}}\big) \right\|_K, \qquad \text{(A11)}\\ |T_6| &\le \left\| \kappa_j^{1/2}\big(\delta\mathcal{P}_{\check{\jmath}}^{j} q_{\check{\jmath}} - \delta\mathcal{P}_{\hat{\jmath}}^{j} q_{\hat{\jmath}}\big) \right\|_K \cdot \left\| \kappa_j^{1/2}\big(\mathcal{P}_{\check{\jmath}}^{j} e_{\check{\jmath}} - \mathcal{P}_{\hat{\jmath}}^{j} e_{\hat{\jmath}}\big) \right\|_K \\ &= \eta_{\mathrm{GM},\mathrm{DF}_\perp,K} \left\| \kappa_j^{1/2}\big(\mathcal{P}_{\check{\jmath}}^{j} e_{\check{\jmath}} - \mathcal{P}_{\hat{\jmath}}^{j} e_{\hat{\jmath}}\big) \right\|_K. \qquad \text{(A12)}\end{aligned}$$

Setting

$$a_K := \left\| \mathcal{K}_i^{1/2}\nabla_i e_i \right\|_K \ (K \in \mathcal{T}_{\Omega_i}), \qquad b_K := \left\| \kappa_j^{1/2}\big(\mathcal{P}_{\check{\jmath}}^{j} e_{\check{\jmath}} - \mathcal{P}_{\hat{\jmath}}^{j} e_{\hat{\jmath}}\big) \right\|_K \ (K \in \mathcal{T}_{\Gamma_j}),$$

the definition of $|||\cdot|||$ in Sect. 3.3 gives the identity $\sum_{i,K} a_K^2 + \sum_{j,K} b_K^2 = |||e|||^2$. Combining the cellwise bounds (A7)–(A12) in (A5) and grouping the right-hand sides by their dependence on a_K or b_K yields

$$\begin{aligned}|||e|||^2 \le \sum_{i,K} \big(\eta_{\mathrm{NM,R},K} + \eta_{\mathrm{GM,R},K} + \eta_{\mathrm{NM},\mathrm{DF}_\parallel,K} + \eta_{\mathrm{GM},\mathrm{DF}_\parallel,K}\big)\, a_K \\ + \sum_{j,K} \big(\eta_{\mathrm{NM},\mathrm{DF}_\perp,K} + \eta_{\mathrm{GM},\mathrm{DF}_\perp,K}\big)\, b_K. \qquad \text{(A13)}\end{aligned}$$

We bound each of the four global indicators of (32) by Cauchy–Schwarz. For the NM residual contributions, $\sum_{i,K} a_K^2 \le |||e|||^2$ gives

$$\sum_{i,K} \eta_{\mathrm{NM,R},K}\, a_K \le \eta_{\mathrm{NM,R}}(\boldsymbol{v}, f)\, |||e|||, \qquad \sum_{i,K} \eta_{\mathrm{GM,R},K}\, a_K \le \eta_{\mathrm{GM,R}}(\boldsymbol{v})\, |||e|||.$$

For the NM diffusive contributions we apply Cauchy–Schwarz *jointly* on the bulk and interface index sets to the $\eta_{\mathrm{NM},\mathrm{DF}_\parallel,K} \sqcup \eta_{\mathrm{NM},\mathrm{DF}_\perp,K}$ and $a_K \sqcup b_K$ vectors:

$$\sum_{i,K} \eta_{\mathrm{NM},\mathrm{DF}_\parallel,K}\, a_K + \sum_{j,K} \eta_{\mathrm{NM},\mathrm{DF}_\perp,K}\, b_K \le \sqrt{\eta_{\mathrm{NM},\mathrm{DF}_\parallel}^2 + \eta_{\mathrm{NM},\mathrm{DF}_\perp}^2} \sqrt{\sum_{i,K} a_K^2 + \sum_{j,K} b_K^2}$$

$$= \eta_{\mathrm{NM,DF}}(q, \boldsymbol{v})\, |||e|||,$$

by definition (33c), and analogously

$$\sum_{i,K} \eta_{\mathrm{GM,DF}_{\parallel},K}\, a_K + \sum_{j,K} \eta_{\mathrm{GM,DF}_{\perp},K}\, b_K \le \eta_{\mathrm{GM,DF}}(q, \boldsymbol{v})\, |||e|||,$$

by definition (33d). Substituting the four bounds back into (A13) and dividing by $|||e|||$ (the case $|||e||| = 0$ being trivial) yields

$$|||p - q||| \le \eta_{\mathrm{NM,R}}(\boldsymbol{v}, f) + \eta_{\mathrm{GM,R}}(\boldsymbol{v}) + \eta_{\mathrm{NM,DF}}(q, \boldsymbol{v}) + \eta_{\mathrm{GM,DF}}(q, \boldsymbol{v}) = \mathcal{M}(q, \boldsymbol{v}, f) =: \mathcal{M}_p^{\oplus},$$

which is the upper bound for the primal variable in part (i) of Theorem 1. □

A.2 Upper bound on the dual variable

We mimic the proof of part (b) of [20, Theorem 5.1, Appendix C], with the additional grid-mismatch contributions arising from the splitting $\mathcal{D} = \widetilde{\mathcal{D}} + \delta\mathcal{D}$ and $\mathcal{P} = \widetilde{\mathcal{P}} + \delta\mathcal{P}$ on the non-matching coupling triplets. Let $\boldsymbol{u} = [\boldsymbol{u}_{0,i}, \lambda_j] \in \mathbf{X}$ be the solution of the dual weak form (Problem 4), and let $(q, \boldsymbol{v}) \in Q_h^g \times \mathbf{X}_{h,\mathrm{LC}}(f)$ be an arbitrary admissible pair. Define the bulk-lifted fluxes

$$\boldsymbol{u}_i := \boldsymbol{u}_{0,i} + \textstyle\sum_{j \in \check{S}_i} \mathcal{R}_j^* \circ \mathcal{D}_j^{\hat{j}} \lambda_j, \qquad \boldsymbol{v}_i := \boldsymbol{v}_{0,i} + \textstyle\sum_{j \in \check{S}_i} \mathcal{R}_j^* \circ \mathcal{D}_j^{\hat{j}} \nu_j,$$

both regarded as elements of $\mathbf{V}_i$ via the continuous lift $\mathcal{R}_j^*$, in agreement with the definition of the dual energy norm $|||\cdot|||_*$ in Sect. 3.3.

Adding the squares of the primal and dual error norms,

$$\begin{aligned} |||p - q|||^2 + |||\boldsymbol{u} - \boldsymbol{v}|||_*^2 &= \sum_{i \in I} (\mathcal{K}_i \nabla_i (p_i - q_i), \nabla_i (p_i - q_i))_{\Omega_i} \\ &+ \sum_{j \in J} \Big(\kappa_j \big(\mathcal{P}_{\check{j}}^j (p_{\check{j}} - q_{\check{j}}) - \mathcal{P}_{\hat{j}}^j (p_{\hat{j}} - q_{\hat{j}}) \big), \mathcal{P}_{\check{j}}^j (p_{\check{j}} - q_{\check{j}}) - \mathcal{P}_{\hat{j}}^j (p_{\hat{j}} - q_{\hat{j}}) \Big)_{\Gamma_j} \\ &+ \sum_{i \in I} \Big(\mathcal{K}_i^{-1} (\boldsymbol{u}_i - \boldsymbol{v}_i), \boldsymbol{u}_i - \boldsymbol{v}_i \Big)_{\Omega_i} + \sum_{j \in J} \Big(\kappa_j^{-1} (\lambda_j - \nu_j), \lambda_j - \nu_j \Big)_{\Gamma_j}. \end{aligned} \tag{A14}$$

The exact pair $(\boldsymbol{u}, \lambda, p)$ inherits from the dual weak form the constitutive relations

$$\mathcal{K}_i^{-1} \boldsymbol{u}_i = -\nabla_i p_i \text{ in } \Omega_i, \qquad \kappa_j^{-1} \lambda_j = -\big(\mathcal{P}_{\check{j}}^j p_{\check{j}} - \mathcal{P}_{\hat{j}}^j p_{\hat{j}} \big) \text{ on } \Gamma_j,$$

which allow the bulk and interface diffusive contributions of (A14) to be rewritten as

$$(\mathcal{K}_i \nabla_i (p_i - q_i), \nabla_i (p_i - q_i))_{\Omega_i} = \Big\| \mathcal{K}_i^{-1/2} (\boldsymbol{u}_i + \mathcal{K}_i \nabla_i q_i) \Big\|_{\Omega_i}^2,$$

$$\big(\kappa_j J(p-q),\, J(p-q)\big)_{\Gamma_j} = \Big\| \kappa_j^{-1/2} (\lambda_j + \kappa_j J(q)) \Big\|_{\Gamma_j}^2,$$

where we abbreviated $J(\cdot) := \mathcal{P}_{\check{j}}^{j}(\cdot)_{\check{j}} - \mathcal{P}_{\hat{j}}^{j}(\cdot)_{\hat{j}}$. Decomposing $\boldsymbol{u}_i + \mathcal{K}_i \nabla_i q_i = (\boldsymbol{u}_i - \boldsymbol{v}_i) + (\boldsymbol{v}_i + \mathcal{K}_i \nabla_i q_i)$ and analogously for the interface piece, expanding the squares, and adding the $|||\boldsymbol{u} - \boldsymbol{v}|||_*^2$ contributions of (A14) yields the algebraic identity (cf. [20, Eq. (C.4)])

$$|||p - q|||^2 + |||\boldsymbol{u} - \boldsymbol{v}|||_*^2 = |||\boldsymbol{v} + \mathcal{K}\nabla q|||_*^2 + 2\,\Theta(p - q, \boldsymbol{u} - \boldsymbol{v}), \tag{A15}$$

where the diffusive functional and the cross term are

$$|||\boldsymbol{v} + \mathcal{K}\nabla q|||_*^2 := \sum_{i \in I} \Big\| \mathcal{K}_i^{-1/2} (\boldsymbol{v}_i + \mathcal{K}_i \nabla_i q_i) \Big\|_{\Omega_i}^2 + \sum_{j \in J} \Big\| \kappa_j^{-1/2} (\nu_j + \kappa_j J(q)) \Big\|_{\Gamma_j}^2,$$

$$\Theta(p - q, \boldsymbol{u} - \boldsymbol{v}) := -\sum_{i \in I} (\boldsymbol{u}_i - \boldsymbol{v}_i, \nabla_i (p_i - q_i))_{\Omega_i} - \sum_{j \in J} \big(\lambda_j - \nu_j,\, J(p - q)\big)_{\Gamma_j}.$$

Applying the mD integration-by-parts formula [1] to the pair $(p - q, \boldsymbol{u} - \boldsymbol{v}) \in H_0^1(\Omega) \times \mathbf{X}$ (in the same form as (A3)) and substituting on Θ,

$$\Theta(p - q, \boldsymbol{u} - \boldsymbol{v}) = \sum_{i \in I} \Big(\nabla_i \cdot (\boldsymbol{u}_i - \boldsymbol{v}_i) - \textstyle\sum_{j \in \hat{S}_i} \mathcal{D}_j^{\check{j}} (\lambda_j - \nu_j),\, p_i - q_i \Big)_{\Omega_i}.$$

The continuous mass-conservation identity $\nabla_i \cdot \boldsymbol{u}_i - \sum_{j \in \hat{S}_i} \mathcal{D}_j^{\check{j}} \lambda_j = f_i$, inherited from the second equation of Problem 4, then reduces the cross term to

$$\Theta(p - q, \boldsymbol{u} - \boldsymbol{v}) = \sum_{i \in I} (r_i,\, p_i - q_i)_{\Omega_i}, \qquad r_i := f_i - \nabla_i \cdot \boldsymbol{v}_i + \textstyle\sum_{j \in \hat{S}_i} \mathcal{D}_j^{\check{j}} \nu_j.$$

Splitting $r_i = \widetilde{r}_i + \rho_i$ as in the primal proof, the discrete part $\widetilde{r}_i$ has zero cell mean by Definition 7 and the grid-mismatch part ρ_i has zero cell mean by Lemma 3. Subtracting the cell mean $\overline{(p - q)_i}^{K}$ on every $K \in \mathcal{T}_{\Omega_i}$ and applying the Poincaré–Wirtinger inequality together with the ellipticity bound from Assumption 2 (exactly as in the bound for T_1 and T_4 in Appendix A.1), then summing cellwise via Cauchy–Schwarz on each indicator separately,

$$\begin{aligned} |\Theta(p - q, \boldsymbol{u} - \boldsymbol{v})| &\le \big(\eta_{\mathrm{NM,R}}(\boldsymbol{v}, f) + \eta_{\mathrm{GM,R}}(\boldsymbol{v})\big) \Big\| \mathcal{K}^{1/2} \nabla (p - q) \Big\|_{\Omega} \\ &\le \big(\eta_{\mathrm{NM,R}}(\boldsymbol{v}, f) + \eta_{\mathrm{GM,R}}(\boldsymbol{v})\big)\, |||p - q|||, \end{aligned}$$

where the second inequality uses $\big\| \mathcal{K}^{1/2} \nabla (p - q) \big\|_{\Omega} \le |||p - q|||$ from the definition of the energy norm $|||\cdot|||$.

By the Young inequality $2ab \le a^2 + b^2$ applied to $a = \eta_{\mathrm{NM,R}}(\boldsymbol{v}, f) + \eta_{\mathrm{GM,R}}(\boldsymbol{v})$ and $b = |||p - q|||$,

$$2|\Theta(p - q, \boldsymbol{u} - \boldsymbol{v})| \le \big(\eta_{\mathrm{NM,R}}(\boldsymbol{v}, f) + \eta_{\mathrm{GM,R}}(\boldsymbol{v})\big)^2 + |||p - q|||^2.$$

Substituting into (A15) and cancelling $|||p - q|||^2$ from both sides yields

$$|||\boldsymbol{u} - \boldsymbol{v}|||_*^2 \le |||\boldsymbol{v} + \mathcal{K}\nabla q|||_*^2 + \big(\eta_{\mathrm{NM,R}}(\boldsymbol{v}, f) + \eta_{\mathrm{GM,R}}(\boldsymbol{v})\big)^2. \tag{A16}$$

Taking square roots and using $\sqrt{a^2 + b^2} \le a + b$ for $a, b \ge 0$,

$$|||\boldsymbol{u} - \boldsymbol{v}|||_* \le |||\boldsymbol{v} + \mathcal{K}\nabla q|||_* + \eta_{\mathrm{NM,R}}(\boldsymbol{v}, f) + \eta_{\mathrm{GM,R}}(\boldsymbol{v}). \tag{A17}$$

It remains to express $|||\boldsymbol{v} + \mathcal{K}\nabla q|||_*$ in terms of the diffusive indicators of Theorem 1. Splitting the continuous transfer operators into their discrete realizations and the corresponding defect operators (Definition 5, with the lift convention (27) on $\widetilde{\mathcal{R}}_j^*$),

$$\begin{aligned}
\mathcal{K}_i^{-1/2}(\boldsymbol{v}_i + \mathcal{K}_i \nabla_i q_i) &= \underbrace{\mathcal{K}_i^{-1/2}\Big(\boldsymbol{v}_{0,i} + \textstyle\sum_{j \in \check{S}_i} \widetilde{\mathcal{R}}_j^* \circ \widetilde{\mathcal{D}}_j^{\hat{\jmath}} v_j\Big) + \mathcal{K}_i^{1/2}\nabla_i q_i}_{\eta_{\mathrm{NM,DF}_\parallel,K} \text{ pointwise on } K} \\
&\quad + \underbrace{\mathcal{K}_i^{-1/2} \textstyle\sum_{j \in \check{S}_i} \widetilde{\mathcal{R}}_j^* \circ \delta\mathcal{D}_j^{\hat{\jmath}} v_j}_{\eta_{\mathrm{GM,DF}_\parallel,K} \text{ pointwise on } K}, \\
\kappa_j^{-1/2}(v_j + \kappa_j J(q)) &= \underbrace{\kappa_j^{-1/2} v_j + \kappa_j^{1/2}\big(\widetilde{\mathcal{P}}_{\check{\jmath}}^j q_{\check{\jmath}} - \widetilde{\mathcal{P}}_{\hat{\jmath}}^j q_{\hat{\jmath}}\big)}_{\eta_{\mathrm{NM,DF}_\perp,K} \text{ pointwise on } K} + \underbrace{\kappa_j^{1/2}\big(\delta\mathcal{P}_{\check{\jmath}}^j q_{\check{\jmath}} - \delta\mathcal{P}_{\hat{\jmath}}^j q_{\hat{\jmath}}\big)}_{\eta_{\mathrm{GM,DF}_\perp,K} \text{ pointwise on } K}.
\end{aligned}$$

Applying the triangle inequality on the product space $L^2(\Omega) \times L^2(\Gamma)$ to the sum of these two contributions yields

$$\begin{aligned}
|||\boldsymbol{v} + \mathcal{K}\nabla q|||_* &\le \sqrt{\sum_{i,K} \eta_{\mathrm{NM,DF}_\parallel,K}^2 + \sum_{j,K} \eta_{\mathrm{NM,DF}_\perp,K}^2} \\
&\quad + \sqrt{\sum_{i,K} \eta_{\mathrm{GM,DF}_\parallel,K}^2 + \sum_{j,K} \eta_{\mathrm{GM,DF}_\perp,K}^2} \\
&= \eta_{\mathrm{NM,DF}}(q, \boldsymbol{v}) + \eta_{\mathrm{GM,DF}}(q, \boldsymbol{v}),
\end{aligned}$$

by the global indicator definitions (33c) and (33d). Substituting back into (A17),

$$\begin{aligned}
|||\boldsymbol{u} - \boldsymbol{v}|||_* &\le \eta_{\mathrm{NM,DF}}(q, \boldsymbol{v}) + \eta_{\mathrm{GM,DF}}(q, \boldsymbol{v}) + \eta_{\mathrm{NM,R}}(\boldsymbol{v}, f) + \eta_{\mathrm{GM,R}}(\boldsymbol{v}) \\
&= \mathcal{M}(q, \boldsymbol{v}, f) =: \mathcal{M}_{\boldsymbol{u}}^{\oplus},
\end{aligned}$$

which is the upper bound for the dual variable in part (ii) of Theorem 1. □

Acknowledgements The authors would like to thank Jan M. Nordbotten for valuable discussions on the topic.

Author Contributions Jhabriel Varela: Conceptualization, Methodology, Software, Validation, Formal Analysis, Writing - Original Draft, Writing - Review & Editing, Visualization; Christian E. Schaerer: Conceptualization, Methodology, Formal Analysis, Project Administration, Funding Acquisition; Eirik Keilegavlen: Conceptualization, Methodology, Software, Writing - Review & Editing; Inga Berre: Conceptualization, Writing - Review & Editing, Project Administration, Funding Acquisition.

Funding Open access funding provided by University of Bergen (incl Haukeland University Hospital). This project has received funding from the European Research Council (ERC) under the European Union's Horizon 2020 research and innovation programme (grant agreement No 101002507). JV was funded by the Paraguayan National Council of Science and Technology (CONACYT) through the program: Advanced Human Capital Insertion in Academia (PRIA01-8). CES was funded by CONACYT project number ESTR01-23 and by SISNI.

Data Availability Code is available for reproduction via the mdnme Python package: jhabriel/non matching estimates: mdnme v0.3, https://doi.org/10.5281/zenodo.17844410.

Code Availability Code is available for reproduction via the `mdnme` Python package [60].

Declarations

Conflict of interest The authors declare no conflict of interest.

Usage of Artificial Intelligence Parts of the software implementation were developed with the assistance of `Claude Code` powered by `Claude Sonnet 4.6`. `ChatGPT 5.5` was used to improve readability of selected parts of the manuscript.

Open Access This article is licensed under a Creative Commons Attribution 4.0 International License, which permits use, sharing, adaptation, distribution and reproduction in any medium or format, as long as you give appropriate credit to the original author(s) and the source, provide a link to the Creative Commons licence, and indicate if changes were made. The images or other third party material in this article are included in the article's Creative Commons licence, unless indicated otherwise in a credit line to the material. If material is not included in the article's Creative Commons licence and your intended use is not permitted by statutory regulation or exceeds the permitted use, you will need to obtain permission directly from the copyright holder. To view a copy of this licence, visit http://creativecommons.org/licenses/by/4.0/.

References

1. Boon, W.M., Nordbotten, J.M., Vatne, J.E.: Functional analysis and exterior calculus on mixed-dimensional geometries. Annali di Matematica **1923**, 757–789 (2021). https://doi.org/10.1007/s10231-020-01013-1
2. Martin, V., Jaffré, J., Roberts, J.E.: Modeling fractures and barriers as interfaces for flow in porous media. SIAM J. Sci. Comput. **26**(5), 1667–1691 (2005). https://doi.org/10.1137/S1064827503429363
3. Nordbotten, J.M., Boon, W.M., Fumagalli, A., Keilegavlen, E.: Unified approach to discretization of flow in fractured porous media. Comput. Geosci. **23**(2), 225–237 (2019). https://doi.org/10.1007/s10596-018-9778-9
4. Berre, I., Doster, F., Keilegavlen, E.: Flow in fractured porous media: a review of conceptual models and discretization approaches. Transp. Porous Media **130**(1), 215–236 (2019). https://doi.org/10.1007/s11242-018-1171-6
5. Formaggia, L., Fumagalli, A., Scotti, A.: Numerical methods for flow in fractured porous media. In: Gupta, H.K. (ed.) Heat and Mass Transfer in Porous Media, pp. 1125–1130. Springer, Cham (2021). https://doi.org/10.1007/978-3-030-58631-7_289

6. Flemisch, B., Berre, I., Boon, W., Fumagalli, A., Schwenck, N., Scotti, A., Stefansson, I., Tatomir, A.: Benchmarks for single-phase flow in fractured porous media. Adv. Water Resour. **111**, 239–258 (2018). https://doi.org/10.1016/j.advwatres.2017.10.036
7. Berre, I., Boon, W.M., Flemisch, B., Fumagalli, A., Gläser, D., Keilegavlen, E., Scotti, A., Stefansson, I., Tatomir, A., Brenner, K., Burbulla, S., Devloo, P., Duran, O., Favino, M., Hennicker, J., Lee, I.-H., Lipnikov, K., Masson, R., Mosthaf, K., Nestola, M.G.C., Ni, C.-F., Nikitin, K., Schädle, P., Svyatskiy, D., Yanbarisov, R., Zulian, P.: Verification benchmarks for single-phase flow in three-dimensional fractured porous media. Adv. Water Resour. **147**, 103759 (2021). https://doi.org/10.1016/j.advwatres.2020.103759
8. Both, J.W., Brattekås, B., Keilegavlen, E., Fernø, M., Nordbotten, J.M.: High-fidelity experimental model verification for flow in fractured porous media. InterPore J. **1**(3), 271124–6 (2024). https://doi.org/10.69631/ipj.v1i3nr31
9. Frih, N., Martin, V., Roberts, J.E., Saâda, A.: Modeling fractures as interfaces with nonmatching grids. Comput. Geosci. **16**(4), 1043–1060 (2012). https://doi.org/10.1007/s10596-012-9302-6
10. D'Angelo, C., Scotti, A.: A mixed finite element method for darcy flow in fractured porous media with non-matching grids. ESAIM: Math. Model. Numer. Anal. **46**(2), 465–489 (2012). https://doi.org/10.1051/m2an/2011148
11. Fumagalli, A., Scotti, A.: A numerical method for two-phase flow in fractured porous media with non-matching grids. Adv. Water Resour. **62**, 454–464 (2013). https://doi.org/10.1016/j.advwatres.2013.04.001
12. Fumagalli, A., Keilegavlen, E.: Dual virtual element methods for discrete fracture matrix models. Oil Gas Sci. and Technol. Revue d'IFP Energies Nouvelles **74**, 41 (2019). https://doi.org/10.2516/ogst/2019008
13. Boon, W.M., Gläser, D., Helmig, R., Yotov, I.: Flux-mortar mixed finite element methods on nonmatching grids. SIAM J. Numer. Anal. **60**(3), 1193–1225 (2022). https://doi.org/10.1137/20M1361407
14. Pencheva, G.V., Vohralík, M., Wheeler, M.F., Wildey, T.: Robust a posteriori error control and adaptivity for multiscale, multinumerics, and mortar coupling. SIAM J. Numer. Anal. **51**(1), 526–554 (2013). https://doi.org/10.1137/110839047
15. Chen, H., Salama, A., Sun, S.: Adaptive mixed finite element methods for Darcy flow in fractured porous media. Water Resour. Res. **52**(10), 7851–7868 (2016). https://doi.org/10.1002/2015WR018450
16. Chen, H., Sun, S.: A residual-based a posteriori error estimator for single-phase Darcy flow in fractured porous media. Numer. Math. **136**(3), 805–839 (2017). https://doi.org/10.1007/s00211-016-0851-9
17. Mghazli, Z., Naji, I.: Guaranteed a posteriori error estimates for a fractured porous medium. Math. Comput. Simul. **164**, 163–179 (2019). https://doi.org/10.1016/j.matcom.2019.02.002
18. Hecht, F., Mghazli, Z., Naji, I., Roberts, J.E.: A residual a posteriori error estimators for a model for flow in porous media with fractures. J. Sci. Comput. **79**(2), 935–968 (2019). https://doi.org/10.1007/s10915-018-0875-7
19. Zhao, L., Chung, E.: An adaptive discontinuous galerkin method for the Darcy system in fractured porous media. Comput. Geosci. **26**(6), 1581–1596 (2022). https://doi.org/10.1007/s10596-022-10171-5
20. Varela, J., Ahmed, E., Keilegavlen, E., Nordbotten, J.M., Radu, F.A.: A posteriori error estimates for hierarchical mixed-dimensional elliptic equations. J. Numer. Math. **31**(4), 247–280 (2023). https://doi.org/10.1515/jnma-2022-0038
21. Gander, M.J., Japhet, C.: An algorithm for non-matching grid projections with linear complexity. In: Bercovier, M., Gander, M.J., Kornhuber, R., Widlund, O. (eds.) Domain Decomposition Methods in Science and Engineering XVIII, pp. 185–192. Springer, Berlin, Heidelberg (2009). https://doi.org/10.1007/978-3-642-02677-5_19
22. Gander, M.J., Japhet, C.: Algorithm 932: PANG: software for nonmatching grid projections in 2D and 3D with linear complexity. ACM Trans. Math. Softw. (TOMS) **40**(1), 1–25 (2013). https://doi.org/10.1145/2513109.2513115
23. McCoid, C., Gander, M.J.: A provably robust algorithm for triangle-triangle intersections in floating-point arithmetic. ACM Trans. on Math. Softw. (TOMS) **48**(2), 1–30 (2022). https://doi.org/10.1145/3513264
24. Boon, W.M., Nordbotten, J.M., Yotov, I.: Robust discretization of flow in fractured porous media. SIAM J. Numer. Anal. **56**(4), 2203–2233 (2018). https://doi.org/10.1137/17M1139102

25. Keilegavlen, E., Berge, R., Fumagalli, A., Starnoni, M., Stefansson, I., Varela, J., Berre, I.: Porepy: an open-source software for simulation of multiphysics processes in fractured porous media. Comput. Geosci. **25**(1), 243–265 (2021). https://doi.org/10.1007/s10596-020-10002-5
26. Evans, L.C.: Partial Differential Equations, vol. 19, 2nd edn. American Mathematical Society, Providence, RI (2022)
27. Taylor, M.E.: Partial Differential Equations I: Basic Theory, vol. 115, 2nd edn. Springer, New York (2011). https://doi.org/10.1007/978-1-4419-7055-8
28. Bastian, P., Buse, G., Sander, O.: Infrastructure for the coupling of dune grids. In: Numerical Mathematics and Advanced Applications 2009: Proceedings of ENUMATH 2009, the 8th European Conference on Numerical Mathematics and Advanced Applications, Uppsala, July 2009, pp. 107–114. Springer (2010)
29. Scott, L.R., Zhang, S.: Finite element interpolation of nonsmooth functions satisfying boundary conditions. Math. Comput. **54**(190), 483–493 (1990). https://doi.org/10.2307/2008497
30. Repin, S.I.: Estimates of deviations from exact solutions of elliptic variational inequalities. Zap. Nauchn. Sem. S.-Peterburg. Otdel. Mat. Inst. Steklov. (POMI) **271**, 188–203317 (2000). https://doi.org/10.1023/A:1023378021130
31. Lions, J.-L., Magenes, E.: Non-Homogeneous Boundary Value Problems and Applications, vol. 1. Springer, Berlin (2012)
32. McLean, W.: Strongly Elliptic Systems and Boundary Integral Equations, vol. 131. Cambridge University Press, Cambridge (2000)
33. Brenner, S.C., Scott, L.R.: The Mathematical Theory of Finite Element Methods, vol. 15, 3rd edn. Springer, New York (2008)
34. Repin, S.I., Sauter, S., Smolianski, A.: Two-sided a posteriori error estimates for mixed formulations of elliptic problems. SIAM J. Numer. Anal. **45**(3), 928–945 (2007). https://doi.org/10.1137/050641533
35. Repin, S.I.: A Posteriori Estimates for Partial Differential Equations, vol. 4, p. 316. Walter de Gruyter GmbH & Co. KG, Berlin (2008). https://doi.org/10.1515/9783110203042
36. Zienkiewicz, O.C., Zhu, J.Z.: A simple error estimator and adaptive procedure for practical engineering analysis. analysis. Int. J. Num. Meth. Eng. **24**(2), 337–357 (1987). https://doi.org/10.1002/nme.1620240206
37. Zienkiewicz, O.C., Zhu, J.Z.: The superconvergent patch recovery and a posteriori error estimates. part 1: the recovery technique. Int. J. Numer. Meth. Eng. **33**(7), 1331–1364 (1992). https://doi.org/10.1002/nme.1620330702
38. Ainsworth, M., Oden, J.T.: A posteriori error estimators for second order elliptic systems. part 2: an optimal order process for calculating self-equilibrating fluxes. Comput. Math. Appl. **26**(9), 75–87 (1993). https://doi.org/10.1016/0898-1221(93)90007-I
39. Ern, A., Vohralík, M.: Polynomial-degree-robust a posteriori estimates in a unified setting for conforming, nonconforming, discontinuous Galerkin, and mixed discretizations. SIAM J. Numer. Anal. **53**(2), 1058–1081 (2015). https://doi.org/10.1137/130950100
40. Smears, I., Vohralík, M.: Simple and robust equilibrated flux a posteriori estimates for singularly perturbed reaction-diffusion problems. ESAIM: Math. Model. Numer. Anal. **54**(6), 1951–1973 (2020). https://doi.org/10.1051/m2an/2020034
41. Cai, D., Cai, Z., Zhang, S.: Robust equilibrated a posteriori error estimator for higher order finite element approximations to diffusion problems. Numer. Math. **144**(1), 1–21 (2020). https://doi.org/10.1007/s00211-019-01075-1
42. Cai, D., Cai, Z.: A hybrid a posteriori error estimator for conforming finite element approximations. Comput. Methods Appl. Mech. Eng. **339**, 320–340 (2018). https://doi.org/10.1016/j.cma.2018.04.050
43. Chen, H., Sun, S.: A residual-based a posteriori error estimator for single-phase Darcy flow in fractured porous media. Numer. Math. **136**(3), 805–839 (2017). https://doi.org/10.1007/s00211-016-0851-9
44. Cochez-Dhondt, S., Nicaise, S., Repin, S.I.: A posteriori error estimates for finite volume approximations. Math. Model. Nat. Phenom. **4**(1), 106–122 (2009). https://doi.org/10.1051/mmnp/20094105
45. Wang, N., Li, M., Ma, R., Zhang, L.: Accuracy analysis of gradient reconstruction on isotropic unstructured meshes and its effects on inviscid flow simulation. Adv. Aerodyn. **1**, 1–31 (2019). https://doi.org/10.1186/s42774-019-0020-9
46. Huang, Y., Jiang, K., Yi, N.: Some weighted averaging methods for gradient recovery. Adv. Appl. Math. Mech. **4**(2), 131–155 (2012). https://doi.org/10.4208/aamm.10-m1188

47. Sozer, E., Brehm, C., Kiris, C.C.: Gradient calculation methods on arbitrary polyhedral unstructured meshes for cell-centered CFD solvers. In: 52nd Aerospace Sciences Meeting, pp. 1440 (2014). doi:https://doi.org/10.2514/6.2014-1440
48. Mavriplis, D.: Revisiting the least-squares procedure for gradient reconstruction on unstructured meshes. In: 16th AIAA Computational Fluid Dynamics Conference, pp. 3986 (2003). doi:https://doi.org/10.2514/6.2003-3986
49. Vohralík, M.: A posteriori error estimates for finite volume and mixed finite element discretizations of convection-diffusion-reaction equations. In: Paris-Sud Working Group on Modelling and Scientific Computing 2006–2007. ESAIM Proc., vol. 18, pp. 57–69. EDP Sci., Les Ulis (2007). doi:https://doi.org/10.1051/proc:071806
50. Vohralík, M.: Unified primal formulation-based a priori and a posteriori error analysis of mixed finite element methods. Math. Comp. **79**(272), 2001–2032 (2010). https://doi.org/10.1090/S0025-5718-2010-02375-0
51. Varela, J., Schaerer, C.E., Keilegavlen, E.: A linear potential reconstruction technique based on Raviart-Thomas basis functions for cell-centered finite volume approximations to the Darcy problem. Proc. Ser. Brazilian Soc. Comput. Appl. Math. **11**(1), 1–7 (2025). https://doi.org/10.5540/03.2025.011.01.0332
52. Aavatsmark, I.: An introduction to multipoint flux approximations for quadrilateral grids. Comput. Geosci. **6**(3–4), 405–432 (2002). https://doi.org/10.1023/A:1021291114475
53. Nordbotten, J.M., Keilegavlen, E.: An introduction to multi-point flux (MPFA) and stress (MPSA) finite volume methods for thermo-poroelasticity. In: Di Pietro, D.A., Formaggia, L., Masson, R. (eds.) Polyhedral Methods in Geosciences, pp. 119–158. Springer, Cham (2021). https://doi.org/10.1007/978-3-030-69363-3_4
54. Reichenberger, V., Jakobs, H., Bastian, P., Helmig, R.: A mixed-dimensional finite volume method for two-phase flow in fractured porous media. Adv. Water Resour. **29**(7), 1020–1036 (2006). https://doi.org/10.1016/j.advwatres.2005.09.001
55. Antonietti, P.F., Formaggia, L., Scotti, A., Verani, M., Verzott, N.: Mimetic finite difference approximation of flows in fractured porous media. ESAIM: Math. Model. Numer. Anal. **50**(3), 809–832 (2016). https://doi.org/10.1051/m2an/2015087
56. Formaggia, L., Scotti, A., Sottocasa, F.: Analysis of a mimetic finite difference approximation of flows in fractured porous media. ESAIM: Math. Model. Numer. Anal. **52**(2), 595–630 (2018). https://doi.org/10.1051/m2an/2017028
57. Antonietti, P.F., Facciolà, C., Russo, A., Verani, M.: Discontinuous Galerkin approximation of flows in fractured porous media on polytopic grids. SIAM J. Sci. Comput. **41**(1), 109–138 (2019). https://doi.org/10.1137/17M1138194
58. Antonietti, P.F., Facciolà, C., Verani, M.: Polytopic discontinuous Galerkin methods for the numerical modelling of flow in porous media with networks of intersecting fractures. Comput. Math. Appl. **116**, 116–139 (2022). https://doi.org/10.1016/j.camwa.2021.08.015
59. Vohralík, M.: Equivalence between lowest-order mixed finite element and multi-point finite volume methods on simplicial meshes. ESAIM: Math. Model. Numer. Anal. **40**(2), 367–391 (2006). https://doi.org/10.1051/m2an:2006013
60. Varela, J.: jhabriel/non_matching_estimates: v0.3: A posteriori error estimates on mixed-dimensional non-matching grids. Zenodo (2026). https://doi.org/10.5281/zenodo.20396170
61. Geuzaine, C., Remacle, J.-F.: Gmsh: a 3-D finite element mesh generator with built-in pre-and post-processing facilities. Int. J. Numer. Meth. Eng. **79**(11), 1309–1331 (2009). https://doi.org/10.1002/nme.2579

Publisher's Note Springer Nature remains neutral with regard to jurisdictional claims in published maps and institutional affiliations.